

N70-40695-  
697

NATIONAL AERONAUTICS AND SPACE ADMINISTRATION

*Space Programs Summary 37-64, Vol. I*

*Flight Projects*

For the Period May 1 to June 30, 1970

**CASE FILE  
COPY**

**JET PROPULSION LABORATORY  
CALIFORNIA INSTITUTE OF TECHNOLOGY  
PASADENA, CALIFORNIA**

July 31, 1970

NATIONAL AERONAUTICS AND SPACE ADMINISTRATION

*Space Programs Summary 37-64, Vol. I*

*Flight Projects*

For the Period May 1 to June 30, 1970

JET PROPULSION LABORATORY  
CALIFORNIA INSTITUTE OF TECHNOLOGY  
PASADENA, CALIFORNIA

July 31, 1970

**SPACE PROGRAMS SUMMARY 37-64, VOL. I**

**Copyright © 1970**

**Jet Propulsion Laboratory  
California Institute of Technology**

**Prepared Under Contract No. NAS 7-100  
National Aeronautics and Space Administration**

## Preface

The Space Programs Summary is a multivolume, bimonthly publication that presents a review of technical information resulting from current engineering and scientific work performed, or managed, by the Jet Propulsion Laboratory for the National Aeronautics and Space Administration. The Space Programs Summary is currently composed of four volumes:

- Vol. I. *Flight Projects* (Unclassified)
- Vol. II. *The Deep Space Network* (Unclassified)
- Vol. III. *Supporting Research and Advanced Development* (Unclassified)
- Vol. IV. *Flight Projects and Supporting Research and Advanced Development* (Confidential)





## Contents

<b>I. Mariner Mars 1971 Project</b>	<b>1</b>
A. Project Description and Status	1
1. Description	1
B. Data Systems	3
1. Mission and Test Video System	3
C. Space Sciences	7
1. TV Data Acquisition for Image Processing	7
D. Guidance and Control	10
1. Attitude Control Performance in the Commanded Turn Mode of Operation	10
2. Canopus Tracker	15
3. Sun Sensors	18
E. Engineering Mechanics	21
1. Introduction	21
2. Materials Support to Improved Television Camera Shutter	22
3. Spacecraft Flight Loads Analysis	24
F. Propulsion	26
1. Pressurant Relief Assembly Studies	26
<b>II. Viking Project, Orbiter System and Project Support</b>	<b>30</b>
A. Project Description and Status	30
1. Description	30
2. Status	31
B. Guidance and Control	31
1. Automatic Sun Occultation—Sun Acquisition Control for the Viking Spacecraft	31
C. Engineering Mechanics	34
1. Thermal Design	34
2. Ground Handling and Assembly Equipment	37
<b>Subject Index</b>	<b>42</b>

## I. Mariner Mars 1971 Project

### A. Project Description and Status

#### 1. Description

The primary objective of the *Mariner* Mars 1971 Project is to place two spacecraft in orbit around Mars that will be used to perform scientific experiments directed toward achieving a better understanding of the physical characteristics of that planet. Principal among these experiments are measurements of atmospheric and surface parameters at various times and locations to determine the dynamic characteristics of the planet. Approximately 70% of the Martian surface will be observed during a minimum of 90 days of orbital operations.

During Mission A, it is planned to map the topography of a large portion of the Martian surface at a resolution significantly higher than that achievable with earth-based methods or by the *Mariner* Mars 1969 spacecraft. In addition, measurements will be made of the composition, density, pressure, and thermal properties of the planet's atmosphere. Other measurements will be directed toward an understanding of Mars' surface temperatures, composition, and thermal properties (particularly at the polar

caps); its apparent lack of internal activity; its mass distribution; and its shape.

During Mission B, data will be sought on time-variable features of the Martian surface associated with the wave of darkening wherein both seasonal and secular changes occur. Also, information on atmospheric structure and gross dynamics will be obtained, as well as information directed toward an understanding of Mars' mass distribution, its shape, and its apparent lack of internal activity.

A capability will exist to redirect goals for either mission to the alternate mission if desired. The two launches are anticipated for May 1971, with arrival at the planet during the following November.

An engineering objective of the project is to demonstrate the ability of the spacecraft to perform orbital operations in an adaptive mode wherein information from one orbital pass is used to develop the operations plan for subsequent orbital passes. Studies indicate a high probability that at least one of the spacecraft will survive the sun occultation period which occurs shortly after the 90-day mission is

completed. This makes it possible to conduct an Extended Mission for about a year after orbit insertion. The Extended Mission will probably consist of one or two data taking sequences per week with the capability of recording and playing back about a half-recorder of data (16 TV frames and 11 min of spectrometer data).

One of the *Mariner* Mars 1971 flight spacecraft will be new, and the other will be the spare flight spacecraft of the *Mariner* Mars 1969 Project modified to meet the requirements of the 1971 missions and to enhance mission reliability. The proof test model spacecraft of the *Mariner* Mars 1969 Project will be modified to become the proof test model for the *Mariner* Mars 1971 Project, to be used

for preliminary testing and as a simulator in support of flight operations. A major modification for the *Mariner* Mars 1971 mission will be the addition of a rocket motor required to decelerate the spacecraft and place it in orbit around Mars.

Separate scientific instrument subsystems will be required to accomplish the television, infrared radiometer, ultraviolet spectrometer, and infrared spectrometer interferometer experiments given in Table 1. The S-band occultation and celestial mechanics experiments will require no additional equipment on the spacecraft.

The television team matrix is given in Fig. 1.

**Table 1. *Mariner* Mars 1971 scientific experiments and principal investigators**

Television		Infrared interferometer spectrometer	
H. Masursky	Team leader	R. A. Hanel	PI/Goddard Space Flight Center
H. Masursky	PI/U.S. Geological Survey	B. J. Conrath	CI/Goddard Space Flight Center
R. Batson	CI/U.S. Geological Survey	W. A. Hovis	CI/Goddard Space Flight Center
W. Borgeson		V. Kunde	CI/Goddard Space Flight Center
M. Carr		G. V. Levin	CI/Biospherics
J. F. McCauley		P. D. Lowman	CI/Goddard Space Flight Center
D. Milton		C. Prabhakara	CI/Goddard Space Flight Center
R. Wildey		B. Schlachman	CI/Goddard Space Flight Center
D. Wilhelms			
J. Lederberg	PI/Stanford University	Infrared radiometer	
E. Levinthal	CI/Stanford University	G. Neugebauer	PI/Caltech
J. B. Pollack	CI/Cornell University	S. C. Chase	CI/Santa Barbara Research Center
C. Sagan	CI/Cornell University	H. Kieffer	CI/UCLA
G. de Vaucouleurs	PI/University of Texas	E. D. Miner	CI/JPL
W. B. Thompson	PI/Bellcomm	G. Munch	CI/Caltech
G. A. Briggs	CI/Bellcomm	Celestial mechanics	
P. L. Chandeysson	CI/Bellcomm	J. Lorell	Team leader
E. N. Shipley	CI/Bellcomm	J. Lorell	PI/JPL
B. Smith	PI/New Mexico State University	J. D. Anderson	CI/JPL
M. E. Davies	CI/Rand Corp.	W. L. Martin	CI/JPL
W. K. Hartmann	CI/Arizona State University	W. L. Sjogren	CI/JPL
N. H. Horowitz	CI/Caltech	I. Shapiro	PI/MIT
R. B. Leighton	CI/Caltech	M. Ash	CI/MIT
C. B. Leovy	CI/University of Washington	W. Smith	CI/MIT
T. B. McCord	CI/MIT	S-band occultation	
B. C. Murray	CI/Caltech	A. Kliore	PI/JPL
R. P. Sharp	CI/Caltech	D. L. Cain	CI/JPL
Ultraviolet spectrometer		G. Fjeldbo	CI/JPL
C. Barth	PI/University of Colorado	B. L. Seidel	CI/JPL
C. W. Hord	CI/University of Colorado		
J. B. Pearce	CI/University of Colorado		
PI = Principal investigator, who is the proposer for each experiment. CI = Co-investigator, who assists the proposer on each experiment. Team leader heads a particular group of PIs and CIs on an experiment where there is more than one PI.			

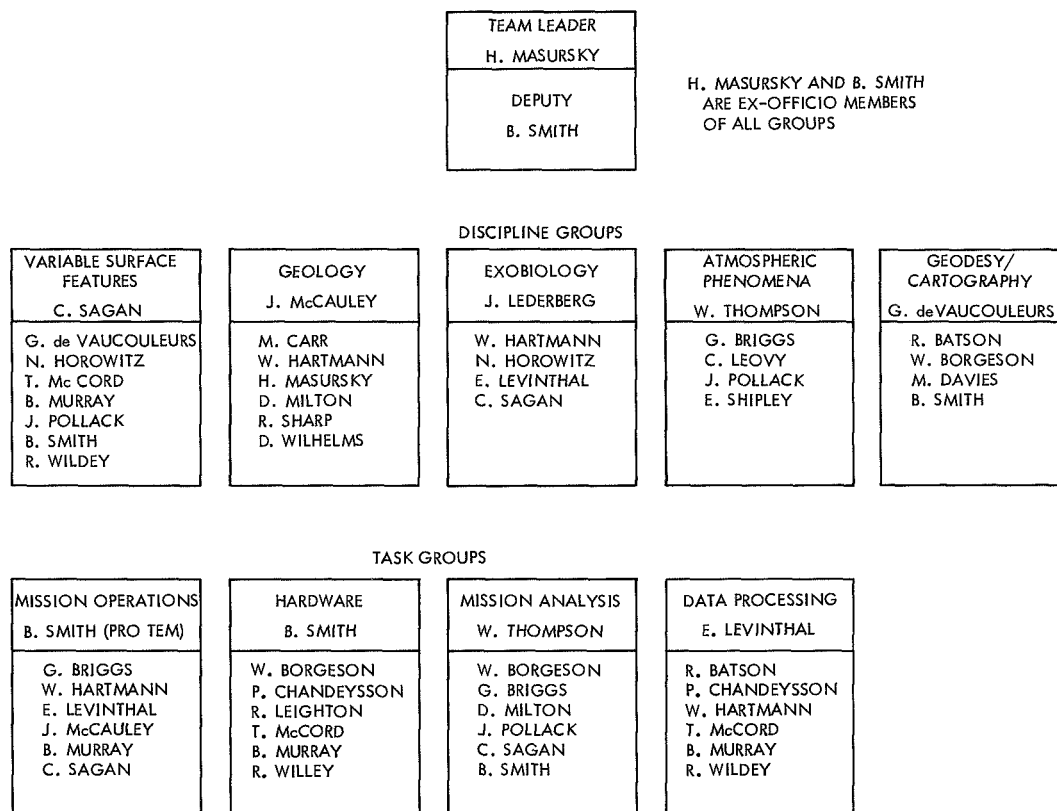


**Fig. 1. Television team matrix**

Management responsibilities for the overall project, the Spacecraft System, the Mission Operations System, and the Tracking and Data System have been assigned to JPL. Lewis Research Center has been assigned management responsibility for the Launch Vehicle System. The launch vehicle will be an *Atlas/Centaur* developed by General Dynamics/Convair.

The *Mariner* Mars 1971 missions will be supported by the Air Force Eastern Test Range launch facilities at Cape Kennedy, the tracking and data acquisition facilities of the Deep Space Network, and other NASA facilities.

## B. Data Systems

### 1. Mission and Test Video System

*a. Introduction.* The mission and test video system (MTVS) is used primarily to receive digital video data from the mission and test computer (MTC) system (SPS 37-63, Vol. I, pp. 4-8) and to produce photographic negatives, prints, and enlargements by the use of film recorders and photoprocessing systems. The data is re-

corded by the MTC system during spacecraft system tests or system-level calibrations of the TV subsystem. Film from other sources, such as the image-processing laboratory or the science support equipment, is also occasionally processed by MTVS.

The MTVS is a development of the *Surveyor* television ground data-handling system, which was modified to handle digital data and otherwise increased in scope to process and display the *Mariner* Mars 1969 flyby video data. Additional expansion and development is being undertaken because the volume of video data processing required for the orbital operations part of the *Mariner* Mars 1971 orbiter spacecraft mission is expected to be vastly increased over that of *Mariner* Mars 1969. About 34,000 total frames per day of photographic hardcopy output are estimated to be required from MTVS during the 90-day orbital operations period. These data types are listed in Table 2. A major portion of the MTVS equipment is located in the JPL SFOF; however, a film recorder and certain photoprocessing equipment is being located in a van directly adjacent to the major equipment area. This van serves as an extension of the available

**Table 2. Estimated MTVS photoproduct output requirements during Mariner Mars 1971 orbital operations period**

Output product	Estimated maximum production time, h	Quantity per video frame	Quantity per plot	Total per day
<sup>a</sup> 70-mm negatives (unmodified data)	3	1		95
<sup>a</sup> 70-mm negatives (modified data)	3	2		190
<sup>a</sup> 70-mm positives	3		1	7000
Strip contact prints	12	3	1	7285
Enlargements				
5 × 7 in.	3	2	As needed	600 max
8 × 10 in.	3	12	As needed	3600 max
11 × 14 in.	12	As needed	As needed	100 max
Duplicate 70-mm negatives	12	6	1	7570
Duplicate 70-mm positives	12	6	1	7570
<sup>a</sup> First-generation copy; negative for video frames; positive for spectral data plots.				

SFOF area, but also will permit relocation of a complete film recording and processing facility at AFETR during the spacecraft launch preparation period.

**b. Photo product output.** The prime MTVS output product is 70-mm film negatives of 55- × 101-mm frame size containing the picture; alphanumeric picture identification data; linear and logarithmic gray scales; and histograms of the raw video data and the displayed video data, which may be a modified version of the raw data. The original negative is used to prepare 70-mm strip-contact prints, and a film positive for producing duplicate negatives, if required.

A typical enlarged frame from the PTM spacecraft TV system test is shown in Fig. 2. The lower left-hand histogram shows the percentage of picture elements (pixels) of each of the 512 possible data number (DN) values in the set of  $5.8 \times 10^5$  picture elements comprising one frame of raw recorded video data. Each 9-bit pixel value is truncated before being output to the 6-bit intensity register of the MTVS film recorder, so the range of values of the film output histogram is 0-63 DN rather than 0-511 DN, as in the input data histogram. The ordinate values in the film output histogram are formed from the averaged sum of the 9-bit pixel DN values taken in successive groups of eight. When the input data is transformed by the MTC system according to any of several options to modify picture contrast or size, the output histogram also reflects these operations. Gray scales which display the density corresponding to each DN level represented in the two histograms are located directly below the appropriate histograms. In addition,

gray scales representing linear and logarithmic changes in DN are shown on the left and right sides of the picture. The logarithmic scale represents input levels of 63, 38, 22, 13, 8, 5, 3, 1, and 0 DN to the film recording system. Picture size may be modified by specifying an arbitrary set of two lines and two pixels which bound the area of the desired "enlarged" picture. This enables close examination of shading and detail, and helps isolate TV subsystem and MTVS problems.

The MTC, by processing other data contained on the same frame-synchronized log tapes as the video data, provides the picture number, data automation system (DAS) time, and camera identification information shown on the data frame. The science or engineering data blocks recorded on tape may also be decommutated and extracted to drive the MTVS film recorder to produce plots of ultraviolet spectrometer (UVS), infrared interferometer spectrometer (IRIS), or infrared radiometer (IRR) instrument data, as well as engineering telemetry data, if desired.

**c. System description.** The total MTVS consists of two film recorders and three transport systems, photoprocessing equipment for film and paper, video data monitors, scan conversion equipment for rendering spacecraft TV data compatible with the RETMA format for display by the SFOF closed-circuit TV (CCTV) system, an interface switching and control system, a small digital computer and peripherals (Honeywell DDP-24), and photographic quality control equipment. Figure 3 shows the block diagram of the equipment located in the mobile van and the SFOF.

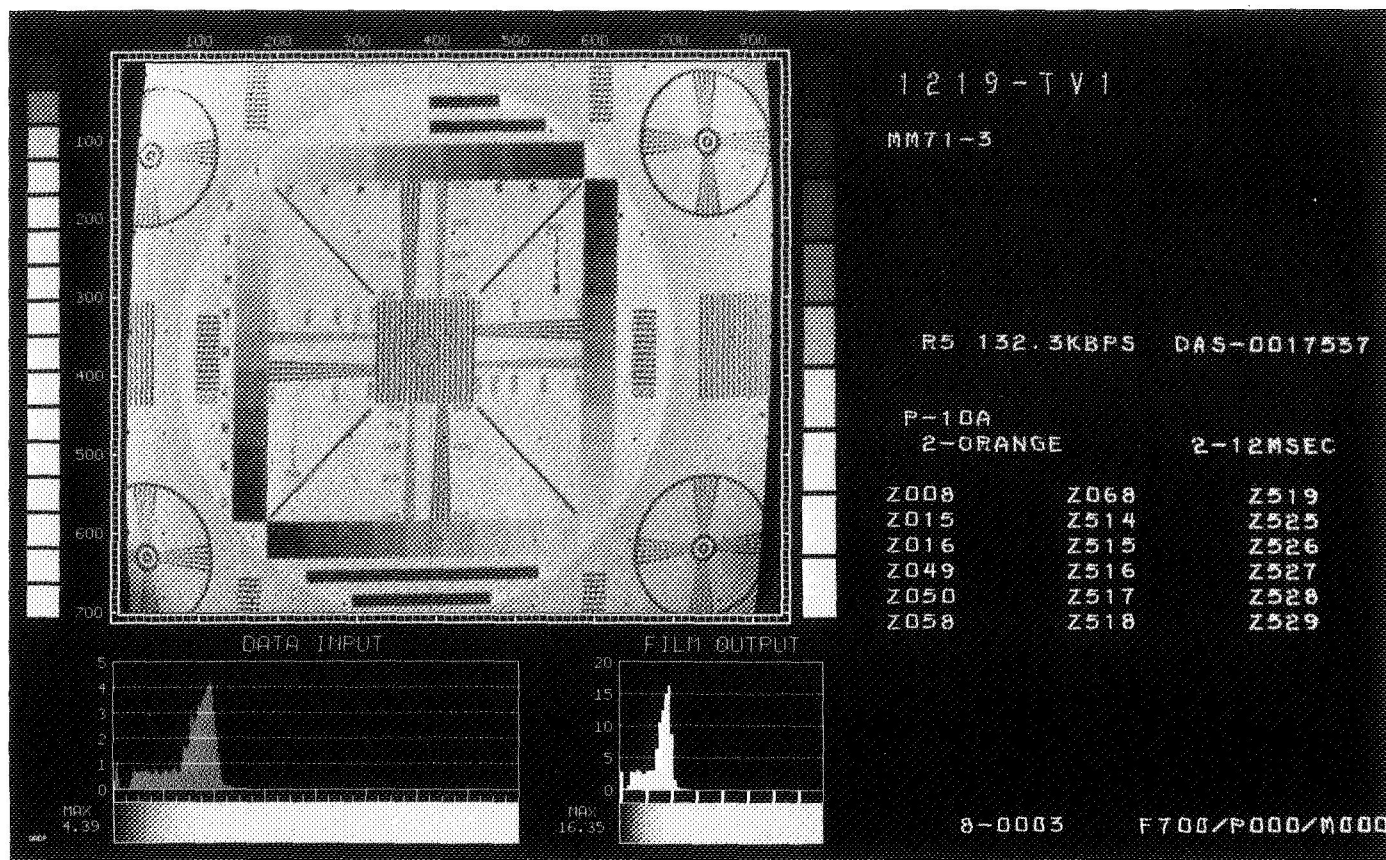


Fig. 2. Typical MTVS 70-mm data frame showing Mariner Mars 1971 TV picture

The film recorders use special 7-in.-round cathode-ray tubes (CRTs) with short-persistence phosphor for generating the 55- × 101-mm data field on the tube face which is photographed by the film transports. High linearity of spot intensity versus input voltage is obtained by the use of optical feedback from a photomultiplier tube which senses the actual CRT light output, and a differential amplifier to compare the photomultiplier output with the system input and correct the difference. Networks for first order correction of geometric distortion are also provided. The spot is positioned on the face of the tube by deflection currents determined by an 11-bit digital-to-analog conversion system, thus providing a 2047 × 2047 element field for the display of the picture, histograms, gray scales, and titles. Transmission of a Y-coordinate and X-coordinate value from the MTC system starts each line of the picture, and a succession of a 6-bit values defines the intensity of each pixel in the line, since the X-position increments automatically with each word transfer. The spot intensity and 7- $\mu$ s shutter (unblanking gate) combine to determine the film exposure for each pixel. The data transfer rate is about 50  $\mu$ s

per word, and a full-field requires about 50 s to complete. Film advance occurs in 500 ms. The present X and Y position converters will shortly be replaced by high-speed digital logic elements to reduce the settling time that now limits the linearity of the system.

Each film recorder is provided with beam splitters that permit the use of two film transports, plus a Polaroid quick-look camera. A total of three transports is currently available. Two different types of data being processed simultaneously may thus be segregated on film according to type. The transports accommodate 1000-ft rolls of 70-mm perforated Mylar-based film.

The density versus exposure characteristic of film used in MTVS photoprocessing can be represented by the plot shown in Fig. 4. Film density  $D$  is the logarithm of reciprocal transmittance (ratio of emergent to incident light intensity). The slope of the approximately linear part of the  $D$  versus log exposure curve shown is called gamma ( $\gamma$ ). Currently, a processing gamma of about 1.8 is used, as defined by the slope of the curve over the

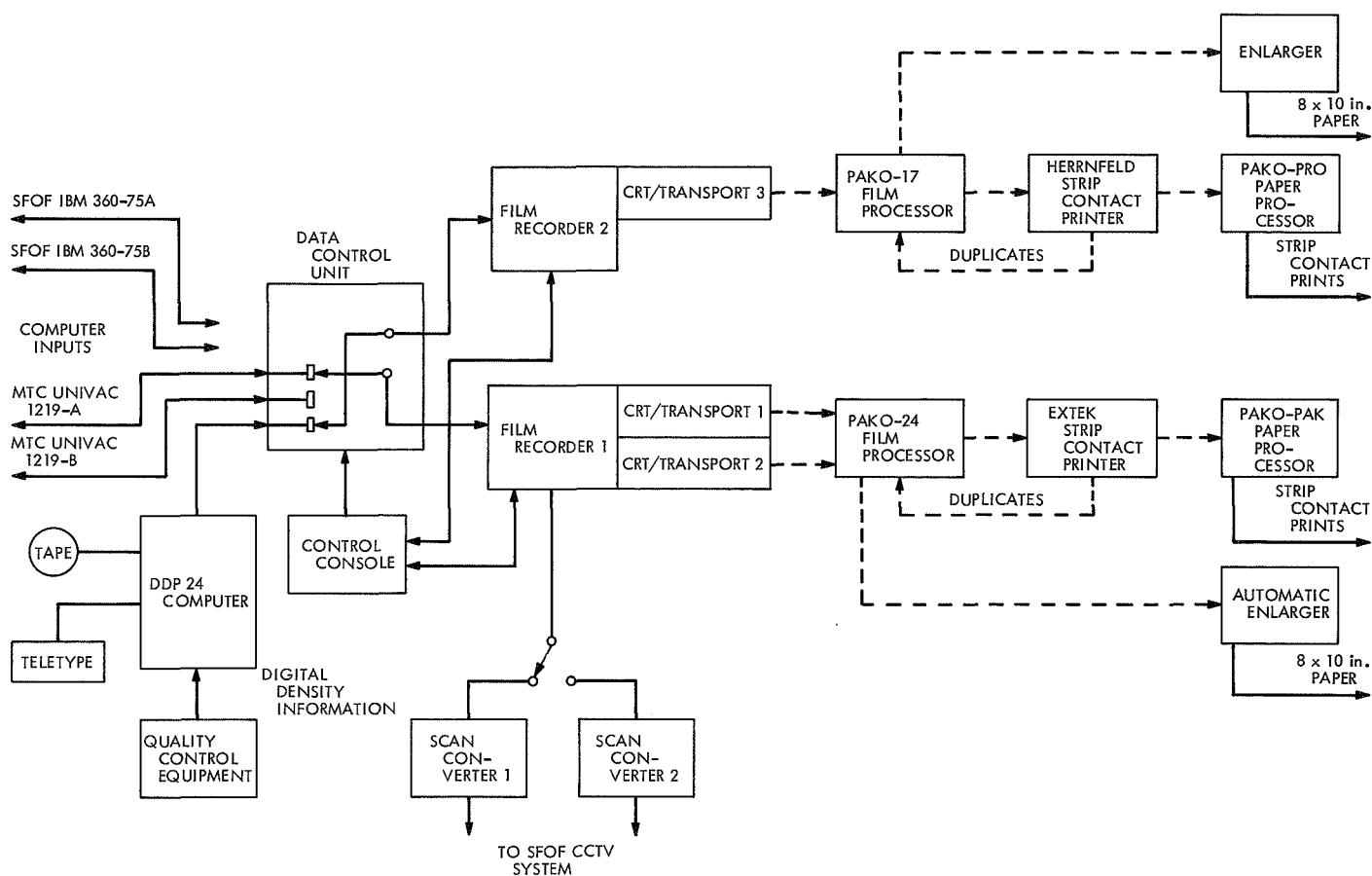


Fig. 3. Block diagram of MTVS equipment configuration

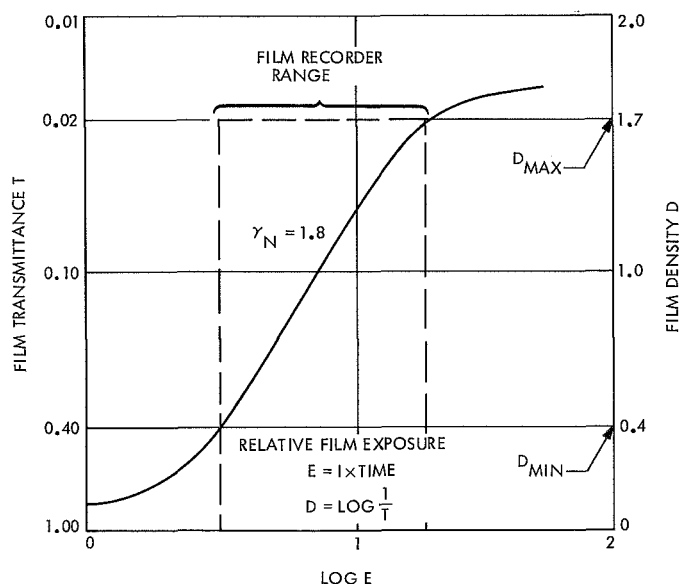
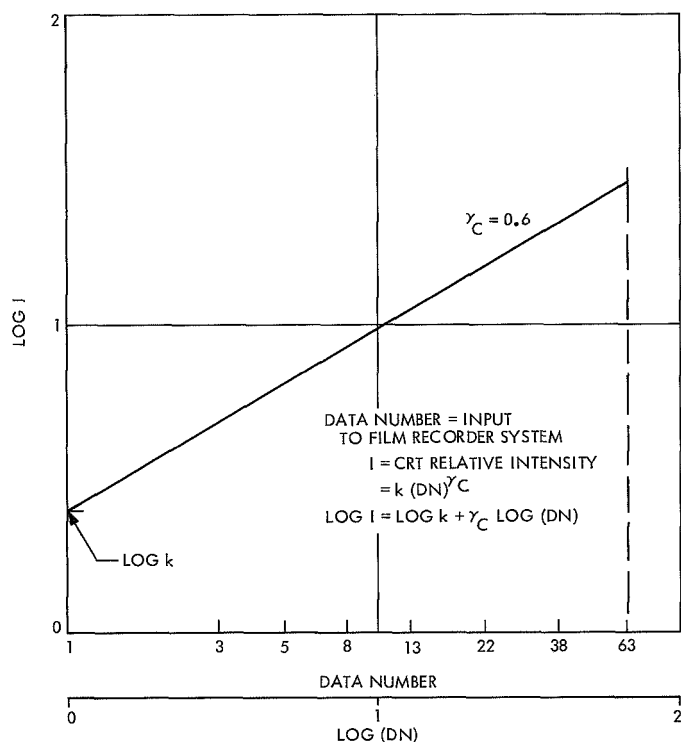


Fig. 4. Density versus exposure characteristic of MTVS film

film density range corresponding to the selected full range of the film recording system, namely  $D_{min} = 0.4$  to  $D_{max} = 1.7$ . This is equivalent to a 20-to-1 contrast (transmittance) ratio. Use of this high film gamma ( $\gamma_N$ ) permits shorter CRT exposure, corresponding to lower spot intensity and consequently decreased spot size. The overall system gamma  $\gamma_s$  is reduced to near unity by a so-called exposure computer preceding the linear film recorder, which introduces a corrective logarithmic function  $\gamma_c$ , such that  $\gamma_s = \gamma_c \gamma_N \cong 1$ , as shown in Fig. 5. This computer can also be set to establish arbitrary levels of  $D_{min}$  and  $\gamma_c$  to compensate for the copying processes required to produce duplicate positives so that the gamma of the final product is near unity. The gray scales shown in Fig. 2 represent the system gamma, whereas processing gamma is determinable only when a gray scale wedge is exposed directly on the film.

Investigations are in process to replace the presently used special-order Eastman film with a much lower cost





**Fig. 5. CRT intensity versus film recorder system input.**  
Exposure computer set at  $\gamma_c = 0.6$

standard film such as GAF Hyscan-B. In turn, the film density range and gamma characteristics to be used will be evaluated to provide the optimum hardcopy product to the user.

A system gamma of unity is desirable if the photocopy is to represent most accurately the contrast of the original scene. This assumes that the light transfer characteristic of the transducer between the original scene and the system input is linear, otherwise the exposure computer may be required to aid in compensating the characteristic of the transducer.

A continuous processor (Pakorol G-24) is used to process cut film or as much as five rolls of 70-mm roll film or semi-opaque positive material (Cronapaque) simultaneously at speeds up to 35 in./min. A somewhat smaller system (Pakorol G-17) is installed in the van but may be relocated near the G-24 unit. A high-speed duplicator for producing 1-to-1 positives, strip-contact prints, and duplicate negatives (Extex duplicator) provides for producing a predetermined number of copies with preprogrammed exposures, at speeds up to 325 ft/min. A 40-ft/min duplicator (Herrnfeld 70-mm strip contact printer) is also installed in the van. Strip contact prints

are processed by Pakopak or Pako-pro paper processors. Most enlargements will be 8- × 10-in. size; however, a 16- × 20-in. capability exists. An automatic roll-paper transport system for the enlargers will provide the capability for producing 500 8- × 10-in. enlargements per hour on 10-in. roll stock. The exposed stock is then processed on the Pako processors.

Photographic quality assurance (QA) is effected using sensitometers, and transmission and reflection densitometers to measure the density (transmittance) or reflectivity of film or paper photoproducts which have been exposed through sensitometric gray-scale wedges. The data obtained is used to set up the exposure computer, select the exposure, processing speed, temperature, and control material acceptance. An investigation of automating the QA process using digital equipment and a proposed file management system for all photo records is in process. The major application of both procedures is in the mission operations phase of the *Mariner Mars 1971* Project.

An electrical interface between the MTVS and the SFOF IBM 360/75 computers will be established for mission operations to enable the Mk III A video system to utilize the MTVS for hardcopy photographic output. Video enhancement or decalibration programs operational in the 360/75 computer may also be able to access the MTVS directly for output.

Work is progressing on development of high-resolution volatile display video monitors with quick-look hardcopy output available within about 30 s of the picture display. These devices would be useful for observing and recording in near real-time the result of several types of computer operations on the video data during mission orbital operations. Functions such as contrast scaling and enlargement are foreseen. Improvements to the scan conversion system for displaying spacecraft video data via the SFOF CCTV subsystem are also being pursued.

## C. Space Sciences

### 1. TV Data Acquisition for Image Processing

**a. Introduction.** The image processing laboratory (IPL) is involved in the processing of video data from the *Mariner Mars 1971* (MM'71) TV system. As part of the calibration of the system the IPL must obtain video data from the TV system during bench calibration tests. It was decided to transfer this data from the bench check-out equipment (BCE) to the IPL directly over a hardware

link and into the IBM 360/44 computer. The BCE also contains a tape recorder, thus providing an additional method of obtaining the data. This data acquisition concept is sufficiently similar to that for the *Mariner Mars 1969* (MM'69) system to allow the hardware built for it to be modified to add a MM'71 mode of operation. The basic data acquisition system has also recently been provided with the added capability of receiving digitized video from a slow-scan TV system. The hardware and the associated software for each of the data acquisition modes (MM'71, MM'69, and slow scan) are described here.

**b. Functional description.** Data from the three sources (MM'71, MM'69, and slow-scan TV) is received by the acquisition hardware over appropriate input lines, changed to a format readily acceptable to the computer, and transferred to it via the IBM 2701 data adapter unit with parallel data adapter (2701-PDA). The 2701-PDA received 16-bit parallel data from the acquisition hardware and presents it to the system/360 input/output (I/O) channel as two 8-bit bytes. A block diagram of the system is shown in Fig. 6.

The MM'71 data input consists of seven data lines and one strobe line. The 6-bit parallel data is derived from the 9-bit picture elements (pixels) as indicated in Table 3. This data and odd parity are gated in the data acquisition equipment by the strobe line. In the equipment a parallel-to-serial conversion is performed, and when 16 bits have been obtained a word is transferred to the 2701-PDA. The input data rate is 22,050 6-bit words/s, and the format is shown in more detail in Table 3. The MM'71 BCE also records the input data on 7-track  $\frac{1}{2}$ -in. computer tape. Provision has been made for handling this data. The digital tape deck associated with the IPL film scanner/recorder has been modified to add the capability of playing back tapes generated by the BCE. Automatic tape controls are included for start and stop commands to minimize the need for operator intervention. The data acquisition system then processes tape identically to the hardline data.

The MM'69 data input is a 13-line interface from the BCE as indicated in Table 3. The acquisition equipment separates the full analog video (FAV) and composite analog video (CAV) data, performs the serial-to-parallel conversion of the digital video (DV) data, and sets the proper line and frame flag. There is also a tape mode which includes deskewing of the 13 data lines before processing.

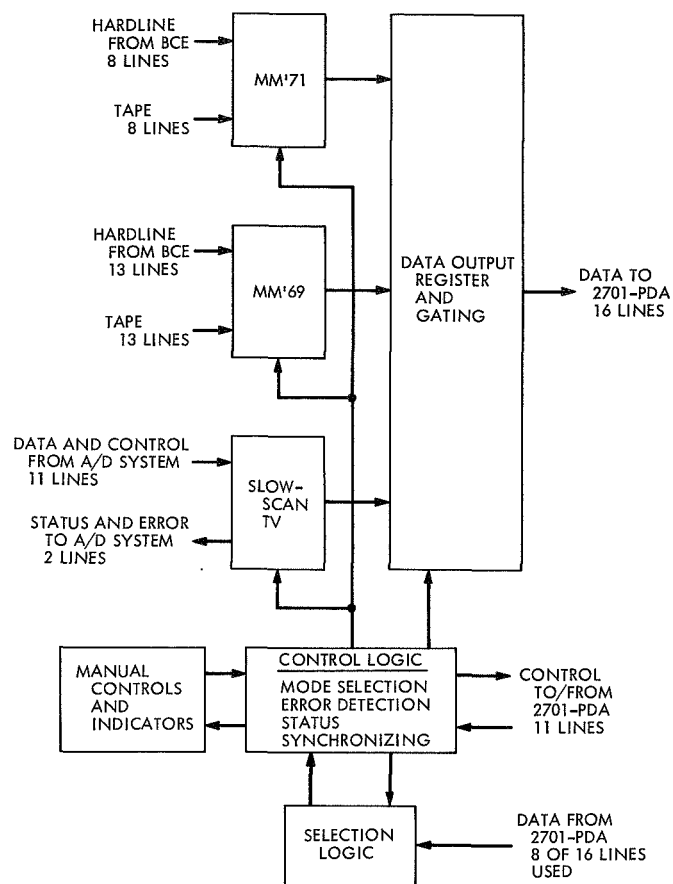


**Fig. 6. TV data acquisition system block diagram**

The recently added slow-scan TV input consists of 11 input lines (8 data, 1 clock, 2 synchronizing) and 2 output lines (status and error). The 8 data lines contain the digital video data which is strobed with each transition of the clock and controlled by synchronizing inputs for line and frame and manual controls.

The analog video is digitized remotely. Clock and synchronizing pulses are also obtained in external equipment. The data acquisition equipment packs two 8-bit picture elements per 16-bit 2701-PDA word and provides the computer with appropriate line and frame indications. The analog-to-digital conversion rate of 500,000 pixels/s exceeds the capability of disk/tape drives on the computer; therefore, the entire picture to be saved must be stored in core. Core restrictions limit the stored picture size to about  $300 \times 300$  elements selected from the entire input. Table 3 summarizes the slow-scan TV interface in somewhat greater detail.

**c. Hardware implementation.** The IPL TV data acquisition hardware is housed in two standard relay racks.

**Table 3. TV data acquisition interface**

MM'71 data interface		
Line	Function	
1-6	6-bit parallel data	
7	Parity (1-7 always contain an odd number of logic ones)	
8	Strobe	
Data rate	22050 6-bit words/s	
Video format	Pixels are 9-bit binary 700 lines per picture (lines and frames identified by PN code and data inserted during retrace time) 832 elements per line	
Data conversion	Two 9-bit pixels are contained in three 6-bit data words on the hardline or three 6-bit characters on tape	
MM'69 data interface		
Line	Function	Comments
1-8	FAV/CAV data	8-bit parallel
9	NRZ sync	Word sync for FAV/CAV data
10	DV data	6-bit serial
11	DV sync	Bit sync for digital video data
12	Line sync	Also provides information for obtaining digital video word sync
13	Frame sync	Level gives camera frame identification, transitions are frame start signals
Data rate	18.9 KHz for NRZ sync, 16.2 KHz for digital video	
Video format	704 lines per picture, 945 elements per line, FAV/CAV data for every element, Digital video data for every 7th element	
Slow-scan data interface		
Line	Function	Comments
1-8	Video data	8-bit parallel
9	Clock	Data strobed with every transition
10	Sync	True during active line time
11	Frame	True during active frame time
12	Error set	Error indication to remote A/D system
13	Ready	Status indication to remote A/D system
Data rate <sup>a</sup>	500 KHz (clock frequency 250 KHz) during active line time	
Video format <sup>a</sup>	Approx. 550 lines per frame Approx. 750 elements per line	
<sup>a</sup> Data rates and video format are not restricted to those indicated. The portion of picture stored is limited to about 300 × 300 elements.		

This includes all input data interfaces; data processing for MM'71, MM'69, and slow-scan TV; data and control interface with the 2701-PDA; manual controls and indicators; and associated mode selection, error detection, and synchronizing logic. The 2701-PDA itself, however, is separate from this hardware. Because other devices besides the data acquisition system are attached to the 2701-PDA input and output buses, addressing and selection logic are included in each device to ensure that only one unit will be activated at a time. Integrated circuit logic is used except for a few special circuits needed. Controls and indicators are grouped functionally, and the most-needed test points are available.

*d. Software for data acquisition.* The detailed programming for the acquisition of data is dependent on which data source is involved. However, the basic method of data transfer is the same for all three sources. Before any data can be transferred, the data acquisition unit must be selected by the 2701-PDA. All units on the output bus monitor the first data word sent by the 2701-PDA. This word contains an address code which all units decode and only the one addressed is enabled. Once the data acquisition unit has been enabled, the program puts the 2701-PDA in the read mode, and the unit then can transfer data to the 360/44 I/O channel via the 2701-PDA on a demand-response basis.

The program for MM'71 data acquisition will receive data from the hardline or tape interface and log this data on disk or tape. Initially the software searches the data, bit by bit, until the PN (pseudonoise) code is found. This PN code, along with other data such as line number and other frame identification information, is sent during horizontal retrace time. Once the first PN code has been obtained, subsequent PNs are verified for proper location and line synchronization is maintained. Only when PNs are not found in the proper location is the bit-by-bit PN search required. The software maintains line and frame sync in the presence of noise by analyzing the frame identification information to minimize the errors comparing the actual data with data expected from an errorless frame. Due to the time necessary for the bit-by-bit PN search, proper line and frame sync may not be obtained if data quality is poor. In this case all the received data can be logged and a second pass can be run off line when more time is available. Normally about 42 s/frame are required for the logging and PN search operations.

In logging MM'69 data a simpler program was required. Line and frame sync were obtained from flag bits set by

the data acquisition hardware. For each picture line of 945 elements, 2059 bytes (8-bit words) of data were recorded. This includes 945 bytes of FAV data, 945 bytes of CAV data, 135 bytes of DV data, and 34 bytes of data derived from the horizontal retrace. Further processing was then necessary for the calibration of the TV system.

The program for data acquisition from the slow-scan TV system produces a formatted and labeled output data set which can be either processed directly or recorded on tape. The specified size parameters are processed to determine the output picture size to be logged, consistent with the size of the input picture and available computer core buffer size. The input data is accumulated in a large buffer through a continuous chained channel program. After completion of the input picture the output data set is written out with the proper label records. Although the frame time is only about 1 s, it takes approximately 30 s to log and format one frame.

## D. Guidance and Control

### 1. Attitude Control Performance in the Commanded Turn Mode of Operation

**a. Introduction.** This article presents the results of an analysis and computer simulation of the *Mariner* Mars 1971 (MM71) attitude-control subsystem in the commanded turn mode of operation. The work was done to verify the new design and to assess the overall performance of the attitude-control subsystem for this control mode. The computer simulation program used the CSSL language for the Univac 1108 computer which was recently developed under the NASA Office of Advanced Research and Technology (OART) Program 125-17-15-10.

During maneuvers and other periods of time when the celestial references cannot be used for providing angular position error information, the attitude-control subsystem operates in the inertial hold mode. On *Mariner* spacecraft prior to MM71, spacecraft angular position information in the inertial mode was obtained by integration of the gyro torquer current by a capacitor network. These capacitors (several parallel capacitors) were physically large and heavy. Recent advances in the state-of-the-art of stable microelectronic devices suggested the use of an active electronic integrator to replace the capacitor network.

Immediate advantages realized with the electronic integrator are: small package size, a reduction in weight, and larger attitude angle storage capability.

**b. Discussion.** The commanded turn sequence for the MM71 spacecraft is roll-yaw. A yaw turn is used instead of a pitch turn to ensure that the scan-platform-mounted science instruments, which in their stowed position view out the yaw axis, will never point at the sun.

An equivalent block diagram of the yaw and roll attitude-control channels for the commanded turn mode is shown in Fig. 7. The control parameters and circuit element values are listed in Table 4. In Fig. 7, the gyro and its associated dynamics are represented as a voltage source  $V_{GY(s)}$ . At initiation of a commanded turn, a precision-regulated voltage source (20 V) with the appropriate polarity is switched on to the integrator input through a resistor T network. The integrator charges up turning on the switching amplifier and firing the  $N_2$  gas valves. The spacecraft accelerates until the gyro signal which is proportional to spacecraft angular rate, produces a steady-state null condition at the integrator and switching-amplifier summing junctions. At this time, the spacecraft has reached its steady-state commanded turn rate  $\dot{\theta}_{CT}$ . During the turn, the integrator, in effect, stores the angular error. Its output voltage is directly proportional to the difference between commanded spacecraft angular position and actual spacecraft angular position.

Referring to Fig. 7, several convenient relationships relating gains, scale factors, and turn rate to the various

**Table 4. Attitude-control commanded turn control parameters and circuit element values**

Control parameter and circuit element	Value	
	Yaw	Roll
$K_{GY}$	402.0 V/rad/s	804 V/rad/s
$V_{cc}$	20.0 V	20.0 V
$\dot{\theta}_{CT}$	0.00316 rad/s	0.00316 rad/s
$i_{db}$	$5.0 \times 10^{-6}$ A	$5.0 \times 10^{-6}$ A
$K_i$	7.80 V/V	6.75 V/V
$R_1$	121 k $\Omega$	243 k $\Omega$
$R_2$	280 $\Omega$	280 $\Omega$
$R_3$	100 k $\Omega$	100 k $\Omega$
$R_4$	38.3 k $\Omega$	38.3 k $\Omega$
$R_5$	1.0 M $\Omega$	1.0 M $\Omega$
$R_T$	266 $\Omega$	266 $\Omega$
$R_G$	196 k $\Omega$	200 k $\Omega$
$R_i$	102 k $\Omega$	51.1 k $\Omega$



and is set at

$$\begin{aligned}\tau &= 4.91 \text{ s (pitch and yaw)} \\ &= 4.19 \text{ s (roll)}\end{aligned}$$

The rate to position gain also establishes the effective rate deadband. For MM71, the inertial hold deadbands are

$$\begin{aligned}\theta_{db} &= \pm \frac{i_{db} R_I}{K_I} \\ &= \pm 0.172 \text{ deg} = \pm 3.0 \text{ mrad (pitch and yaw)} \\ &= \pm 0.086 \text{ deg} = \pm 1.50 \text{ mrad (roll)}\end{aligned}\quad (8)$$

$$\begin{aligned}\dot{\theta}_{db} &= \pm \frac{\theta_{db}}{\tau} \\ &= \pm 0.611 \text{ mrad/s (pitch and yaw)} \\ &= \pm 0.358 \text{ mrad/s (roll)}\end{aligned}\quad (9)$$

The nominal commanded turn rate  $\dot{\theta}_{CT}$  is related to the attitude-control system parameters as follows:

During a commanded turn, the total current at the switching amplifier input is

$$I(s) = -\frac{K_1 R_2 K_{GY} \dot{\theta}(s)}{R_g(R_2 + R_T)} + \frac{1}{C_1 R_I s} \left[ \frac{-R_2 K_{GY} \dot{\theta}(s)}{R_1(R_2 + R_T)} + \frac{V_o}{R_o s} \right]\quad (10)$$

where

$V_o \triangleq$  Thevenin equivalent source for commanded turn voltage  $V_{cc}$

$$= \frac{R_4}{R_3 + R_4} V_{cc} = 5.539 \text{ V}\quad (11)$$

$R_o \triangleq$  Thevenin equivalent source impedance for  $V_{cc}$

$$= R_5 + \frac{R_3 R_4}{R_3 + R_4} = 1.028 \text{ M}\Omega\quad (12)$$

Solving for angular rate  $\dot{\theta}(s)$  yields

$$\dot{\theta}(s) = \frac{V_o(R_2 + R_T)}{s R_1 R_2 R_o C_1 K_{GY} \left( \frac{K_1 s}{R_g} + \frac{1}{R_I R_1 C_1} \right)}\quad (13)$$

In the steady state  $\dot{\theta}(s) = \dot{\theta}_{CT}$ . Applying the final value theorem for Laplace transforms yields

$$\dot{\theta}_{ss} = \dot{\theta}_{CT} = \lim_{s \rightarrow 0} s \dot{\theta}(s) = \frac{V_o(R_2 + R_T) R_1}{R_2 R_o K_{GY}}\quad (14)$$

Substituting the values from Table 4 yields for the nominal turn rate

$$\dot{\theta}_{CT} = 0.181 \text{ deg/s} = 3.16 \text{ mrad/s}$$

The weight of attitude-control gas consumed for commanded turns depends on the gas valve on-time required to accelerate the spacecraft up to turn rate at the beginning of the turn, and to decelerate the spacecraft to zero rate at the end of the turn. Gas consumption is given by

$$W_g = \frac{F}{I_{sp}} t_{on}\quad (15)$$

where

$F$  = gas jet thrust level

$I_{sp}$  = gas specific impulse

$t_{on}$  = valve on-time

For nominal full gas system operation, the valve on-time required to accelerate the spacecraft to turn rate or decelerate from turn rate is simply given by

$$t_{on} = \frac{\dot{\theta}_{CT}}{\alpha_c}\quad (16)$$

where  $\alpha_c$  is the attitude-control subsystem angular control acceleration, and for gas jets functioning in couples is given by

$$\alpha_c = \frac{2FL}{I}\quad (17)$$

where

$F$  = gas jet thrust level

$L$  = gas jet lever arm

$I$  = spacecraft moment of inertia about the turn axis

Previous *Mariner* spacecraft exhibited longer valve on-times for commanded turns due to lower control system damping inherent in their integrating capacitor mechanizations. The lower damping in the earlier designs resulted in large overshoots and greater settling times that resulted in longer valve on-times than given by Eq. (16). However, if a half-gas system failure should occur, the angular control acceleration is cut in half, resulting in some degradation in commanded-turn performance. This is because control system damping during a turn also depends on the magnitude of the angular control acceleration  $\alpha_c$ . A reduction in  $\alpha_c$  causes actual spacecraft position to lag further behind commanded position. This means that the integrator must store a larger angular error which gives rise to turn overshoots and larger settling time. In the case of MM'71, a half-gas system failure does not affect a roll turn, since the  $\alpha_c$  for roll has been sized for roll control during engine firings and is initially twice as large as the  $\alpha_c$  for pitch and yaw. Although not a problem, a yaw turn will exhibit some degradation under the conditions of a half-gas system failure. An approximate relationship for calculating the yaw axis valve on-time can be derived from Eq. (10). Taking the inverse Laplace transform of Eq. (10) and noting that the first switch-off after initiation of the turn occurs when

$$\dot{i}(t) = i_{db}$$

and that

$$\dot{\theta}(t) = \alpha_c t$$

$$\theta(t) = \frac{1}{2}\alpha_c t^2$$

yields

$$\begin{aligned} & \frac{R_2 K_{GY} \alpha_c}{2(R_2 + R_T) R_1 R_I C_1} t_{on}^2 \\ & + \left[ \frac{R_2 K_{GY} K_1 \alpha_c}{(R_2 + R_T) R_G} - \frac{V_o}{R_o R_I C_1} \right] t_{on} - i_{db} = 0 \end{aligned} \quad (18)$$

where for yaw

$$\alpha_c = 0.00045 \text{ rad/s}^2 \text{ (full system)}$$

$$= 0.000225 \text{ rad/s}^2 \text{ (half system)}$$

Substituting in Eq. (18) for the half-system case and solving for  $t_{on}$  for total valve on-time yields

$$T_{on} = 2t_{on} = 38.0 \text{ s}$$

The results presented in the foregoing discussion were verified by computer simulation and are discussed in the following section.

**c. Computer simulation.** To assess the design and performance of the MM'71 attitude-control subsystem in the commanded turn mode of operation, a single-axis computer simulation of the yaw and roll axis attitude-control channels was made, using the CSSL language for the Univac 1108 computer that was recently developed under the NASA OART Program 125-17-15-10. The simulation included all elements of the actual hardware design.

Figures 8a, 9a, and 10a show the pertinent attitude-control and spacecraft response characteristics for a yaw-axis commanded turn of 22.5 deg under nominal full gas system operation. Based on a turn rate of 0.181 deg/s (Eq. 14), the commanded turn voltage (Fig. 7) is applied for 124.25 s. Figures 8a and 9a, which show spacecraft yaw angular rate and position, indicate the high degree of damping inherent in this mechanization. Contrary to the earlier *Mariner* commanded-turn mechanizations, which exhibited large overshoots, the desired commanded-turn rate and deceleration from this rate at completion of the turn is accomplished without overshoot. In fact, this response is considered overdamped since the attitude-control gas jets switch from a hard-on condition to a joggling or intermittent firing condition just prior to the spacecraft reaching its steady-state turn rate. Spacecraft yaw position during the turn is shown in Fig. 9a. The desired turn magnitude of 22.5 deg is achieved within the inertial hold deadband accuracy of the system (0.17 deg). The integrator output voltage during the turn is shown in Fig. 10a. This voltage is proportional to spacecraft angular error (Eq. 2) during the turn and shows that actual spacecraft yaw position is lagging 1.05 deg behind commanded position during the steady-state portion of the turn. For longer duration commanded turns, the steady-state integrator output voltage will undergo excursions of 1.0 V peak-to-peak (2.15 to 3.15 V) during a yaw turn and 0.5 V peak-to-peak (2.0 to 2.5 V) during a roll turn. This variation corresponds to the position limit cycle deadband excursions during the turn. At the end of the turn, the integrator is storing precisely the system deadband error.

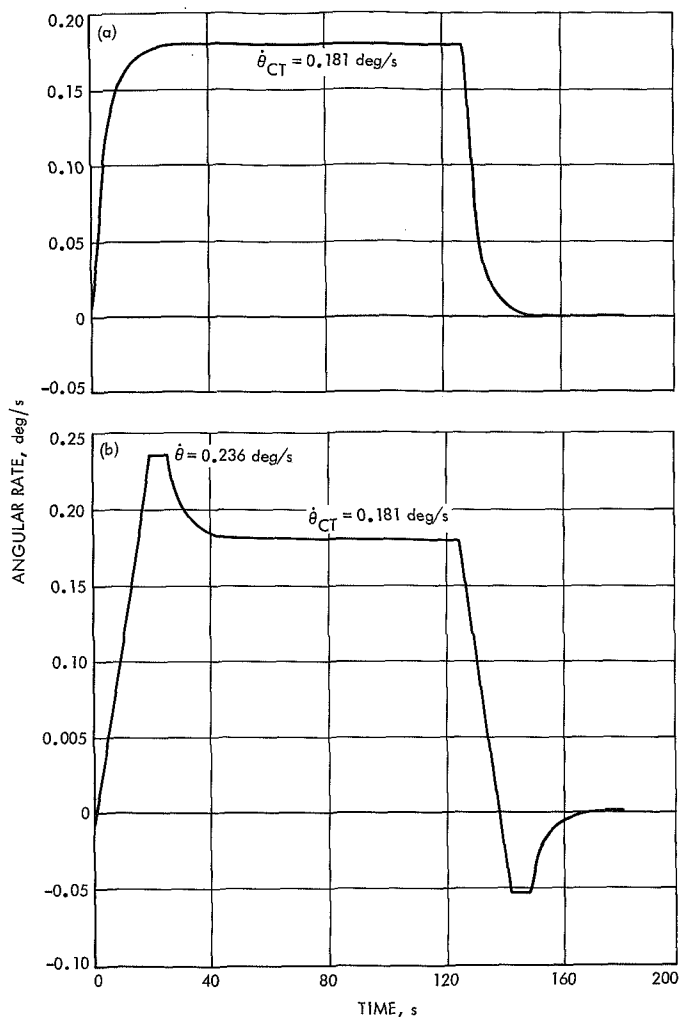


**Fig. 8. Angular rate versus time for yaw turn: (a) full gas system, (b) half gas system**

Figures 8b and 9b show spacecraft rate and position for the same yaw turn under a half-gas system failure condition. If a half-gas system failure should occur (valve failing to open), the gas system angular control acceleration is cut in half, which causes some degradation in yaw turn performance. The spacecraft angular rate and position during the yaw turn show that the response is now somewhat underdamped. Angular position, shown in Fig. 9b, exhibits a small amount of overshoot before settling to the desired turn magnitude. System operation with the lower angular control acceleration requires that the integrator store a greater equivalent angular error. Figure 10b shows that the peak angular error stored on the integrator is 1.45 deg. This is well within the capability of the system, since the integrator storage capability is set at  $\pm 6.0 \text{ deg}$  ( $\pm 18.0 \text{ V}$ ). The integrator storage capability is actually sized to accommodate the autopilot

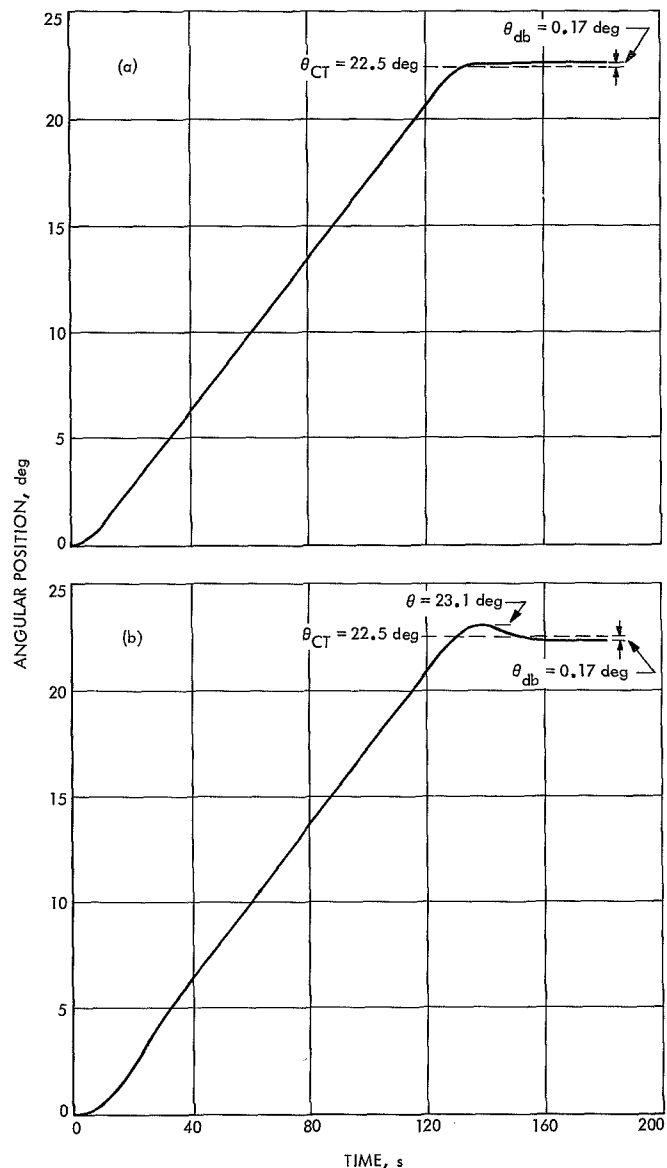


**Fig. 9. Angular position versus time for yaw turn: (a) full gas system, (b) half gas system**

function during powered flight phases where much larger angular storage requirements can arise.

Computer simulation of the attitude-control performance for roll commanded turns provided the same results shown for yaw turns, with the exception that no degradation occurs under half-gas system operation. The reason for this is that the gas-jet thrust levels for the roll axis are sized to provide sufficient roll control torque during powered flight phases of the mission. The resulting angular control acceleration is approximately twice that for pitch and yaw, so that even under half-gas



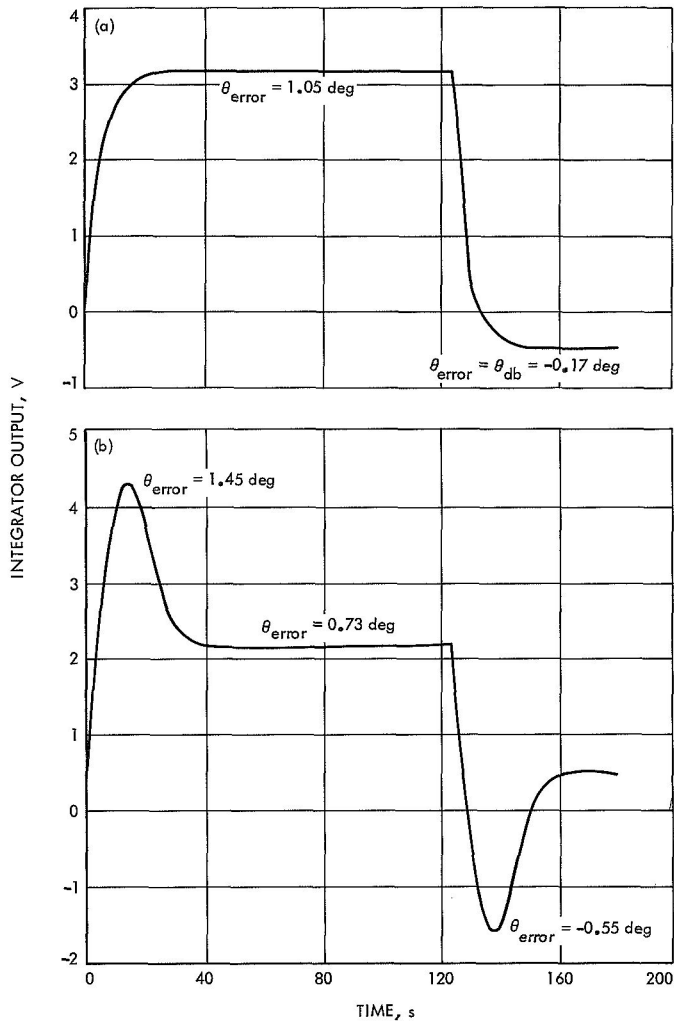


**Fig. 10. Integrator output for yaw turn: (a) full gas system, (b) half gas system**

system operation, roll turns will exhibit highly damped behavior.

**d. Conclusion.** The analysis and computer simulation described in this article was done to assess the design and overall performance of the MM'71 attitude-control subsystem in the commanded turn mode of operation.

The results indicate greatly improved performance over earlier *Mariner* mechanizations from the standpoint of attitude-control response and angular storage capability. Under half-gas system failure conditions, a very small degradation in commanded turn performance is created for yaw turns. Due to the larger angular control acceleration in roll, no effect on roll turn performance is caused by a half-gas system failure.

Due to the high degree of attitude-control system damping attitude control gas consumption is significantly lower for commanded turns. Although commanded-turn gas consumption for the MM'71 spacecraft will be only a very small fraction of the total gas requirement, future missions such as *Viking*, which are planning on performing large numbers of spacecraft turns for mapping and surveillance, will realize significant gas weight saving with this mechanization.

## 2. Canopus Tracker

**a. Introduction.** The *Mariner* Mars 1971 (MM'71) star tracker (Fig. 11) provides roll error signals referenced to the star Canopus, to maintain spacecraft roll-attitude control. Roll-attitude stabilization is required (along with sun sensor derived pitch and yaw stabilization) for a celestial orientation from which midcourse corrections are made and to correctly orient the high-gain antenna during cruise and planet orbit.

The design of the MM'71 Canopus tracker has been changed only slightly from the design of the *Mariner*

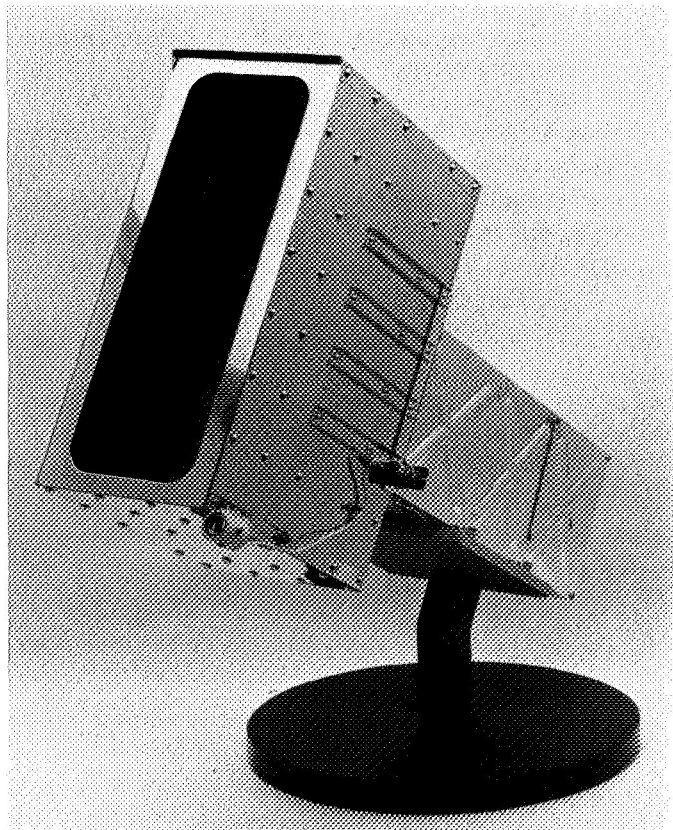


**Fig. 11. *Mariner* Mars 1971 Canopus tracker**

Mars 1969 (MM'69) Canopus tracker. Design improvements derived from MM'69 tracker performance and a few minor design changes for the purpose of increased reliability have been incorporated.

Descriptions of the *Mariner* series Canopus tracker mechanization, testing and flight performance are given in Ref. 1. SPS 37-58, Vol. I, pp. 20-29 provides the theory of operation of the MM'69 Canopus tracker, which is also applicable to the MM'71 tracker.

**b. New design requirements.** The interplanetary phase of the MM'71 mission imposes no new requirements on Canopus tracker operation. The encounter phase, however, has been changed from a MM'69-type flyby to a planet orbital mission. During portions of certain planetary orbits, part of the planet will enter the straylight field of view of the Canopus tracker. The planet straylight can cause the tracker to produce erroneous position errors and, in some cases, could cause loss of Canopus acquisition. In order to prevent these spacecraft roll position perturbations during times of straylight interference, the spacecraft will be placed on inertial roll control. Subsequent to straylight interference, the roll control will be switched back to the tracker. In order to ensure reacquisition of Canopus without a complete spacecraft roll, the tracker will be commanded to perform a scan of its field of view in order to locate and acquire the star. A design change was necessary to the tracker to allow an outside command signal to cause the Canopus tracker to perform a "flyback and sweep" function. The MM'69 tracker had the provision to perform a flyback-and-sweep function directed by internal logic only. With the MM'71 modification, the Canopus tracker will scan, locate, and acquire any object (meeting the intensity gate criteria), within its field of view, on a command from the attitude-control electronics (ACE).

The only other required design changes to the MM'71 tracker included three circuit interfaces with the ACE. The ACE was completely redesigned for the MM'71 mission, and the resulting interface voltages of the adaptive gate step (DC-12) and the star acquisition signal were too high. The tracker circuits were modified for compatibility with the ACE. An impedance change in the gate override circuit (DC-15) was also made.

**c. Review of MM'69 performance.** A review of all problem/failure reports generated on the MM'69 tracker indicated a need for tracker redesign in three areas.

The single most serious problem encountered prior to launch was associated with image dissector noise (high dark current). The effects of tube noise on tracker operation are: (1) limitation of roll angle output accuracy, (2) introduction of error into the star intensity output, and (3) spurious roll angle outputs when tracker logic is disabled (DC-15). "Dark current" within the image dissector is principally composed of leakage current along dielectric surfaces contaminated with cesium deposits. The design approach taken to solve this problem was threefold: (1) the operating voltages on the ID tube were reduced, (2) changes were made to tracker circuitry to make it less susceptible to tube noise, and (3) the tube manufacturer made a slight change to tube processing, which subsequently proved to reduce the dissector noise.

The tracker modifications included controlling the dissector high voltage at 1000 V with a Canopus intensity star input. High voltage with no optical input (dark) was reduced to a maximum of 1500 V due to a correlation between high voltage and high dissector noise.

In the MM'69 tracker design, the gain of the preamplifier was held constant while the dissector dynode voltage was adjusted to provide the required overall preamplifier tube gain. This was necessary since the image dissector gain varies between individual image dissectors. With low-gain dissectors, this method required 1400 to 1500 V on the dissector with a Canopus intensity star input. In the MM'71 design, the gain differences between dissectors is compensated for by selectively adjusting the gain of the preamplifier.

A modification was made to the demodulator circuit to prevent demodulator saturation by the dissector noise fed through the preamplifier. This change includes a diode limiter network placed between the preamplifier and the demodulator. The diode limiter prevents noise bursts generated in the dissector from saturating the roll loop demodulator. Saturation of this demodulator causes erroneous outputs which translate into roll error signals inaccuracies.

A third design change was made by the image dissector manufacturer.<sup>1</sup> This included reportioning the amount of cesium deposited in the area of the dynode structure. This change plus a general improvement in the tube subassembly cleaning procedures was effected to

---

<sup>1</sup>CBS Laboratories, Stamford, Conn.

reduce tube-generated ac noise. Test results have shown the expected reduction in dissector noise levels has been achieved.

An investigation of the Canopus tracker cone-angle update circuitry was also performed. This investigation was prompted by the anomalies exhibited on the *Mariners I* and *II* Canopus tracker cone-angle update events during flight. The circuit design and electronic component application was examined in detail. Although the basic design was found to be satisfactory, there were several areas where improvement was needed. These areas included: revised relay fabrication processes, inspection criteria, and screening tests. The circuit changes included replacement of wet slug capacitors with solid tantalum type and the addition of an integrator circuit to the input of the relay driver circuit to prevent inadvertent triggering by spurious drive pulses. These changes provide the necessary increased confidence in the reliability of the MM'71 cone angle update circuitry.

Many problems were occasioned and much test time was lost during tests of the MM'69 Canopus trackers due to the inadequate magnetic shielding of the image dissector. Investigations into shielding for the MM'71 tracker revealed very poor magnetic field attenuation by the MM'69 shields, probably due to poor annealing of the conetic material. To alleviate this problem, the manufacturing tolerances of the shield were relaxed, so that proper annealing would not take the shield out of tolerance. A new manufacturer was also selected. The new shield has greatly improved magnetic field attenuation, which is apparent from an absence of magnetic interference with operation of the MM'71 trackers.

**d. Minor design changes.** The MM'69 tracker design incorporated the use of eleven Fairchild  $\mu$ A 709 operational amplifiers. JPL electronic component application specialists recommended changing to National Semiconductors LM101AH operational amplifiers for the following reasons: (1) reduction of compensation components, (2) higher gain, (3) built-in short-circuit protection, (4) lower power consumption, (5) lower offset currents, and (6) higher differential input characteristics. The recommendation was accepted, and the change was made to the tracker. The only unusual problem encountered in the use of the LM101AH's was the frequency response of the tracker preamplifier. Since the LM101 has lower frequency response than the  $\mu$ A 709, it was necessary to decrease the frequency compensation capacitor to the limit of 3 pF. With this change, the pre-

amplifier operated at sufficiently high gains without introducing excessive phase shift.

There were a sufficient number of circuit changes to cause a slight packaging problem. This fact, along with existing cable interference problems on circuit board 3, necessitated the repackaging of board 3.

During Canopus tracker engineering prototype tests, a large (10-A, 200  $\mu$ s) turn-on transient was discovered. The cause of this transient was traced to the low-voltage transformer secondary. Since a current spike this large could permanently damage the power-on relay in the ACE, the Canopus tracker transformer was redesigned. The design was changed from a toroidal core to a wound-ring type split toroid with a  $\frac{1}{2}$ -mil air gap. The new design was completely successful in eliminating the 10-A turn-on transient.

Circuit stress analysis revealed the current requirements of the low-voltage diode quad (FSA 1513) to be approximately 90% of the components maximum current rating. The specification was revised to require higher current capabilities, from which new components were then procured.

The MM'71 design philosophy requires the use of fuses in the power lines of all "non-mission-critical" flight equipment. The Canopus tracker was defined as non-mission critical (i.e., its loss would not necessarily be catastrophic to mission success). Fuses were installed in both the tracker and sun shutter 2400-kHz power lines to protect the spacecraft against a tracker power supply failure.

A minor redesign was accomplished in the area of the tracker adaptive gate circuitry. The previous design had two minor faults: (1) the adjustment of all three adaptive gate thresholds were interrelated and, therefore, extremely difficult to properly adjust, and (2) the telemetry readout of the adaptive gate position was only two data numbers (DN) between discrete gate positions. With the addition of an extra voltage divider network, the adjustment of the three adaptive gates is now independent of one another and the telemetry scaling was expanded to provide at least 8 DN between gate positions.

**e. Tracker performance.** Two MM'71 Canopus trackers have been fabricated and tested by the sensor contractor.<sup>2</sup>

---

<sup>2</sup>Honeywell Radiation Center, Lexington, Mass.

In addition, a MM'69 unit was retrofitted and tested to MM'71 design. No generic design problems of any significance have been brought to light during any functional or environmental test sequences. All of the design modifications made for the MM'71 Canopus tracker have been demonstrated to improve tracker performance characteristics or reduce manufacturing difficulties.

### 3. Sun Sensors

*a. Introduction.* The *Mariner Mars 1971* (MM'71) spacecraft uses the same celestial references for attitude control as did the *Mariner Mars 1969* (MM'69), i.e., the sun for pitch and yaw and the star Canopus for roll references. The sun sensors provide error signals enabling the attitude-control system to regulate gas jets which rotate the spacecraft to maintain or alter its attitude as required by the mission. The MM'71 sun sensors, consisting of cruise sensor, acquisition sensor, and sun gate, are structurally simplified forms of the sensors used on the MM'69 spacecraft. The MM'69 sun sensors were documented in SPS 37-53, Vol. I, pp. 34-39.

Due to structural differences between the MM'71 and the MM'69 spacecraft, the sun sensor locations are different. The MM'69 spacecraft was equipped with two pedestal-mounted sensors on the sunlit side of the octagon structure and four sensors on its shadowed side. In this configuration, the spherical-field-of-view requirements were met. The MM'71 mission requires a spacecraft with

larger fuel tanks, which restrict the fields of view in most prospective sun-sensor mounting locations. New locations with adequate fields of view were selected and the sensors designed to mount at these stations. The cruise sensors and sun gate are located on the bay III solar panel outrigger, while the acquisition sensors are located on each of the four solar panel tips (Fig. 12).

The MM'71 design of the sun sensors has significantly altered the sensor configuration and slightly modified their characteristics, while their basic principle of operation remains unchanged. The redesign includes the use of materials with the ability to withstand severe cold temperature cycles. Also included in redesign is a reduction in the scale factor of the sensors and a modified output curve.

*b. Theory of operation.* The set of sun sensors which provides pitch and yaw axis error signals to the attitude-control system of the MM'71 spacecraft consists of the following (Fig. 13):

- (1) A cruise sensor sensitive in the pitch and yaw axes, with a relatively narrow primary field of view ( $\pm 20$  deg).
- (2) A pair of acquisition sensors for both the pitch and yaw axes of the spacecraft with a combined two-axes field of view of slightly less than  $4\pi$  sr.
- (3) A sun gate used to switch the acquisition sensors out of operation when the spacecraft's  $-Z$  axis is within approximately 5 deg of the sun line.

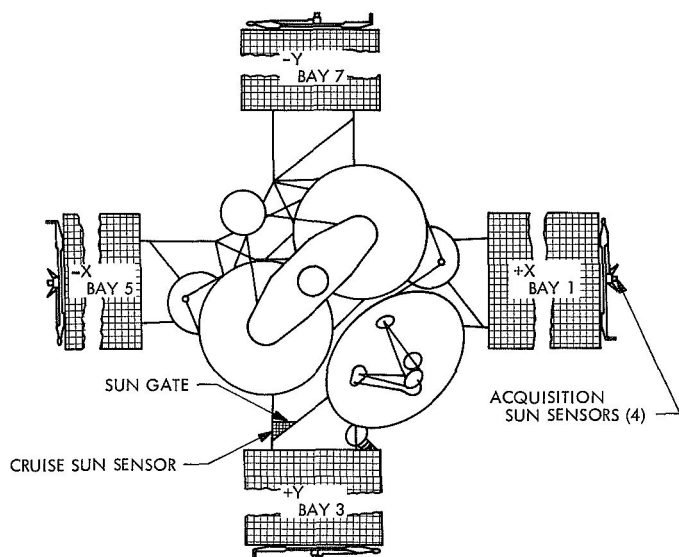
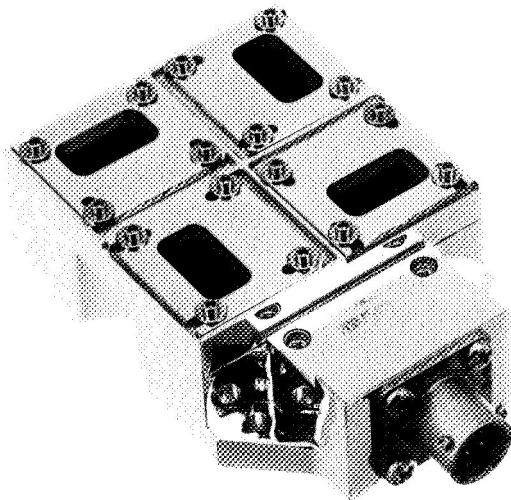
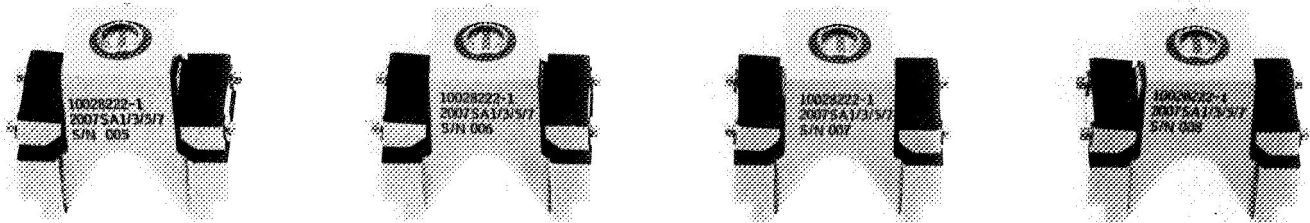


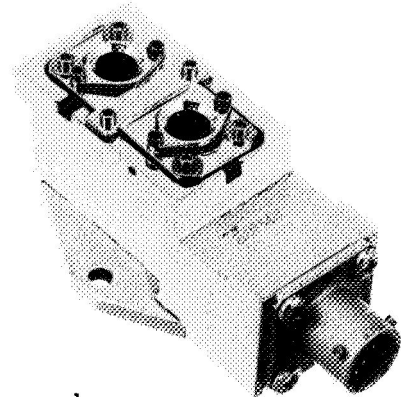
**Fig. 12. Locations of sun sensors on the *Mariner Mars 1971* spacecraft**

The cruise sensor uses the balanced bridge detector principle (Fig. 14). Two cadmium sulfide photoconductors are paired and precisely located beneath bars, which partially shadow their sensitive elements from the sun. A detector fully illuminated at 8400 ft-cd ( $\frac{2}{3}$  solar constant above earth atmosphere), has a resistance of approximately  $750 \Omega$ . When fully shadowed, the resistance exceeds  $20 M\Omega$ . Direct current excitation is applied to the detector pair and produces a zero sensor output voltage when the sun is directly on the zero reference line (equal detector resistance produces balanced bridge). Moving the sensor off the reference line results in a differential action of the shadows, which unbalances the illuminated areas of the detectors and results in an output voltage. The output voltage versus displacement angle is linear to the degree illustrated in the typical output curve of Fig. 15. The scale factor is 4.75 V/deg.

# ACQUISITION SENSORS



CRUISE SENSOR



SUN GATE

Fig. 13. Sun sensors for *Mariner Mars 1971* spacecraft

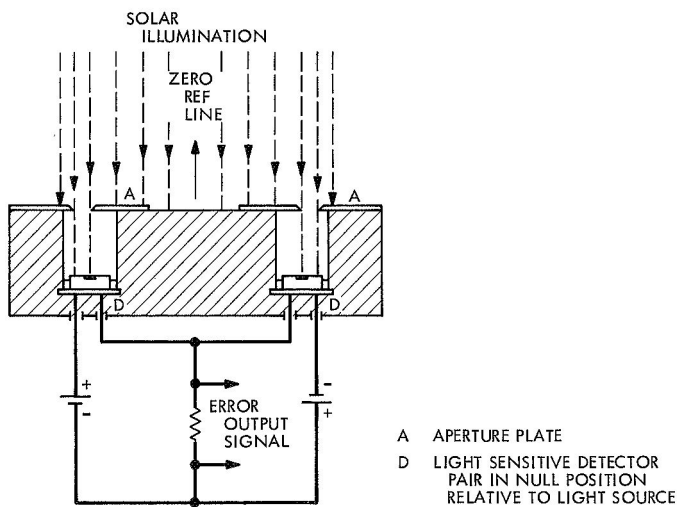


Fig. 14. Electro-optical schematic of the principle used in the cruise and acquisition sensors

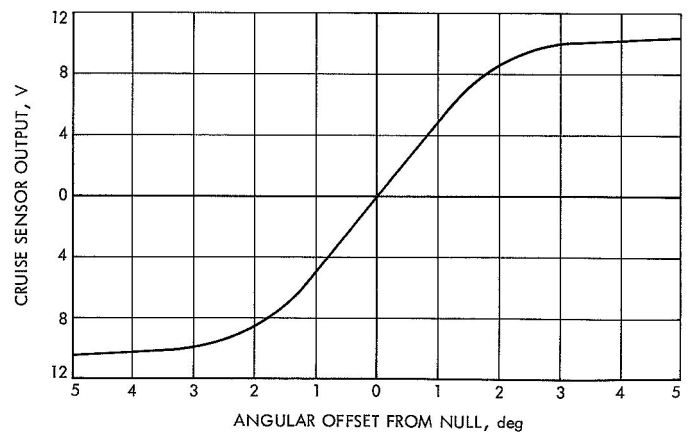


Fig. 15. Cruise sensor output on a single axis (typical curve)

The acquisition sensors consist of four units, each with three detectors mounted as shown in Fig. 16. The four acquisition sensors cover a  $4\pi$  sr field of view and act basically as a switch. Whenever a detector or group of detectors is solar-illuminated, the attitude-control electronics responds by driving the spacecraft in a direction that will align the cruise sensor with the sun. The acquisition sensors are electrically removed from the sun sensor circuitry, by action of the sun gate, whenever the spacecraft is aligned within 5 deg of the sun. This action prevents degradation of the cruise sensor output by the acquisition sensors which could introduce null errors from their less precise outputs.

The sun gate uses two photoconductors identical to those in the sun sensors; however, they are not in a bridge circuit and function as variable resistors only. The detectors are electrically connected in parallel to increase the sun-gate reliability by use of redundancy. The attitude-control electronics supplies the sun gate with excitation voltage and has circuitry which triggers at a set level of current passed through the variable resistance of the photodetectors.

The sun gate has a conical field of view of 22 deg total included angle, which is centered about the spacecraft roll ( $-Z$ ) axis. As the spacecraft moves to acquire the sun, the sun-gate detectors begin to be illuminated at 11 deg sun offset, and the photodetector resistance decreases rapidly until at 5 deg, the switching of the attitude-control electronics occurs.

*c. Configuration on the spacecraft.* The cruise sensor on the MM71 spacecraft is mounted on the outrigger at bay III, between the octagon structure and the solar panel. At this location, its primary field of view is unobstructed. The primary field of view is centered on the sunline and is a 40-deg total included angle, measured in the pitch and yaw axes. At angles of 22 deg in pitch and 28 deg in yaw, obstructions do exist. Simulation of the worst-case obstruction has shown the reflected light measured at the sun sensor to be 25 ft-cd. Tests show that 25 ft-cd of straylight do not create a null offset while the cruise sensor is aligned to the sun.

The sun gate is mounted beside the cruise sensor and is subject to similar moderate environmental conditions. Its field of view is unobstructed at this location.

The acquisition sensors, because of their large field of view requirements (each sensor has a field of view of approximately 180 by 120 deg), have been moved to the tips of the solar panels. Here they are secured to the gas jet manifold assemblies by brackets. The spacecraft location of the acquisition sensors subject them to wide temperature excursions during the normal mission. Materials with compatible thermal coefficients over a range of  $+131$  to  $-103$  deg are used.

#### d. Design

*Cruise sensor.* Figure 13 shows the physical size and configuration of the cruise sensor. Its modified CL705 cadmium sulfide photoconductors are fitted in glass-filled Teflon bushings and mounted in the aluminum base. The

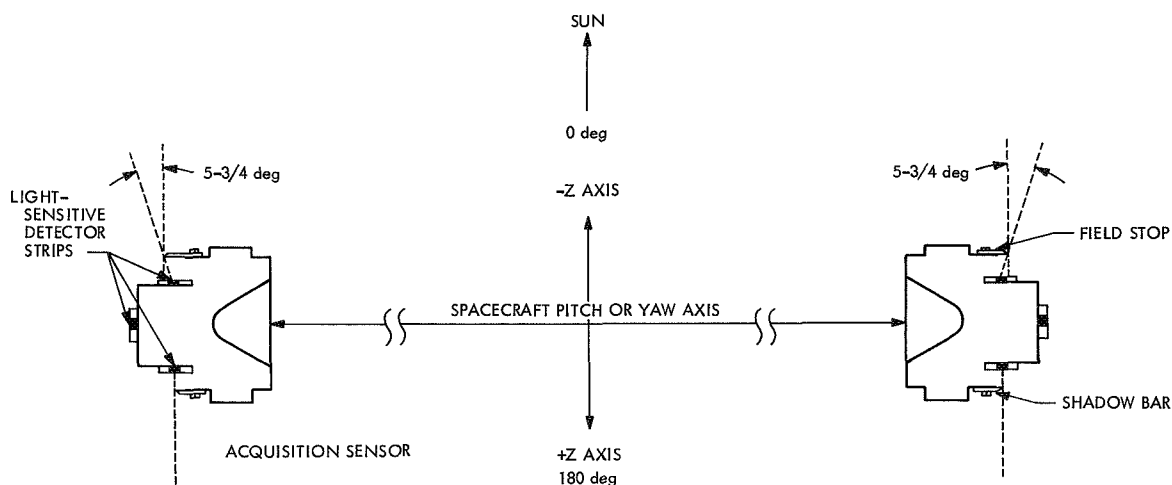


Fig. 16. Acquisition sensor pair showing field stop and shadow bar settings

bushings cushion the detectors against mechanical and thermal stresses without the alignment inaccuracy of more resilient mountings. Further isolation from these stresses is obtained by the application of silicone rubber to the rear surfaces of the TO-5 cans containing the detectors. This mounting configuration maintains overall sensor pointing accuracies at better than  $\pm 4.6$  arc min. The detectors are fabricated with leads of sufficient length to solder directly to the connector, eliminating the need for interconnecting wires. A four-pin connector provides all electrical connections to the unit. The components are secured by filling the underside of the base with Stycast 2850GT/11, which also contributes to the sensors durability.

**Acquisition sensors.** Figure 13 illustrates the size and configuration of the acquisition sensors, and Fig. 16 sketches the mechanical arrangement of the detectors in relation to their shadowing elements. Figure 17 shows the sensor interconnection, in simplified form, as used on the spacecraft.

The three detectors in each acquisition sensor are electrically connected in parallel. When the spacecraft -Z

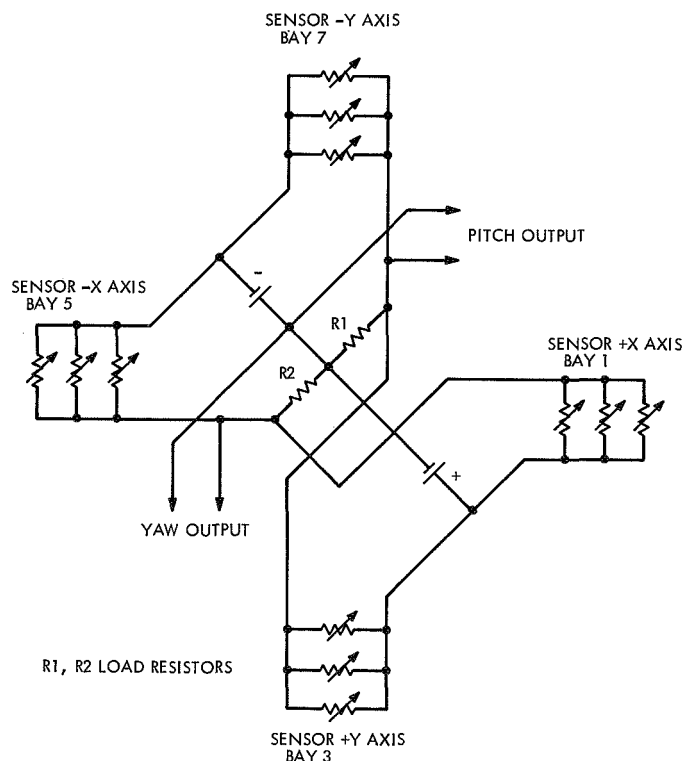


Fig. 17. Acquisition sensors wiring diagram

axis is aligned with the sun, the field stop overshadows the center of the detector strip by  $5\frac{3}{4}$  deg, raising its resistance to approximately  $7000\ \Omega$ . This higher resistance reduces the degradation of the null if sun-gate switching fails to remove the acquisition sensor from the circuit.

As the acquisition sensor rotates about the sunline, its resistance rapidly decreases and remains substantially constant until it nears  $180$  deg, at which point the shadow bar permits illumination of one half the detector strip. The resistance of a half-illuminated detector strip is approximately  $2750\ \Omega$ , where in combination with the second sensor of the pair, it produces an unstable null.

The detector mounting is similar to that used in the cruise sensor; however, a terminal board, rather than a connector, is used for electrical connections, due to the small size of the sensor.

**Sun gate.** The sun gate, which performs a sensing function only, is slightly changed from the MM'69 design. A connector replaces the terminal board formerly used, and the body sides have been thermally painted. Internally, a modified detector mounting is fitted with glass-filled bushings.

**e. Testing.** The flight sensors successfully underwent environmental tests of vibration, temperature, and thermal shock and retained their accuracy of performance. The acquisition sensors were thermal-shocked over the temperature range of  $+167$  to  $-148^\circ\text{F}$ .

All flight sensors were calibrated and functionally tested, using natural sunlight of approximately 8400-ft-cd intensity, at the Table Mountain test facility located at an altitude of 7500 ft, in Wrightwood, Calif.

## Reference

1. Goss, W. C., "The Mariner Spacecraft Star Sensors," *App. Optics*, Vol. 9, p. 1056, May, 1970.

## E. Engineering Mechanics

### 1. Introduction

During the reporting period, delivery of *Mariner Mars 1971* (MM'71) flight equipment to the subsystems and the systems test area has continued. Special emphasis has also been placed on supporting problem investigations



and solutions. The results of one such effort, the TV shutter design, is discussed. The results of the MM'71 flight loads analysis is presented. This effort, which resulted in revised structural design criteria, was instrumental in allowing residual *Mariner* Mars 1969 (MM'69) equipment to be used in MM'71.

## 2. Materials Support to Improved Television Camera Shutter

Two failures occurred during developmental testing of shutters for the MM'71 narrow-angle television camera. The failures occurred at  $-50^{\circ}\text{C}$  and were due to fatigue of the mating leading edges of the shutter blades. Fatigue was caused by vibration during operation together with high stresses and mating interference caused by differential thermal contraction at the  $-50^{\circ}\text{C}$  operating temperature.

The television shutter materials and mechanisms used on MM'71 are based on the successful design employed on MM'69. A major design change was the employment of a double lip on one of the shutters (referred to as the female shutter) to improve the light stopping capability of the shutters in the closed position. The configuration and installation of the shutter blades are shown in Fig. 18.

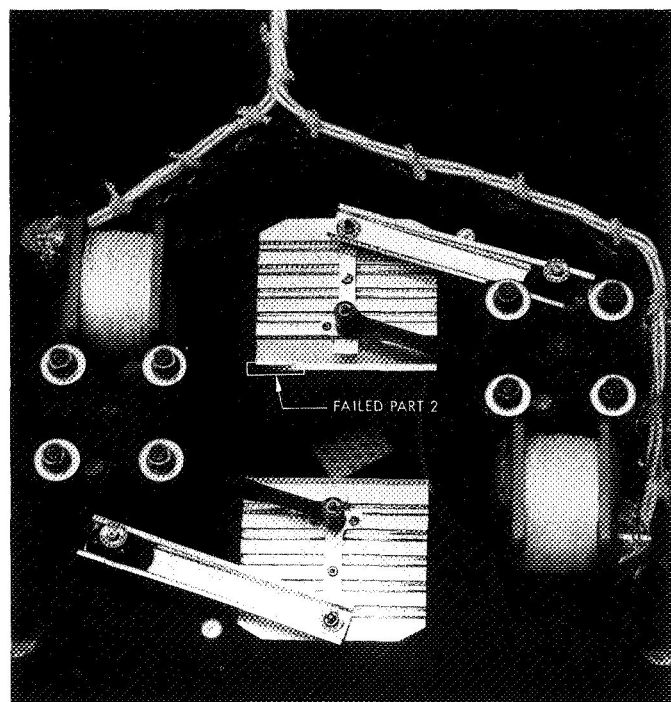


Fig. 18. TV shutter assembly showing failed part 2

The early MM'71 shutter blades were fabricated from Type 1100-H14 aluminum (99% aluminum, Federal Specification QQ-A-250/1). The design incorporated a corrugated construction of the aluminum foil (bend radii 0.020 in. minimum) to give rigidity in the direction normal to shutter movement. Reinforcement "keels" were attached to the shutter blades with rivets to provide rigidity in the shutter movement direction and to provide attachment points. The shutter blades were black-anodized on the camera side to reduce stray light reflections.

*a. Failure analyses.* The failed parts are shown in Figs. 18 and 19. Details about the failed parts are listed in Table 5. Figure 18 shows part 2 after failure, installed in the shutter assembly.

The two failed parts were subjected to extensive failure analyses. The steps taken in the failure analyses and the results are summarized in Table 6. Conclusions drawn from the data of Table 6 were as follows:

- (1) The specified alloy (Type 1100 aluminum) and the optimum grain direction (normal to bend radii) were used.
- (2) The bend radii were not excessively small, and forming procedures were satisfactory because no cracks were observed by fluorescent penetrant inspection.
- (3) The calculated tensile stress in an 0.0026-in. thick aluminum shutter blade at  $-50^{\circ}\text{C}$  was 10,000 psi. This is an overstressed condition when compared with the 7000-psi fatigue endurance limit allowable.

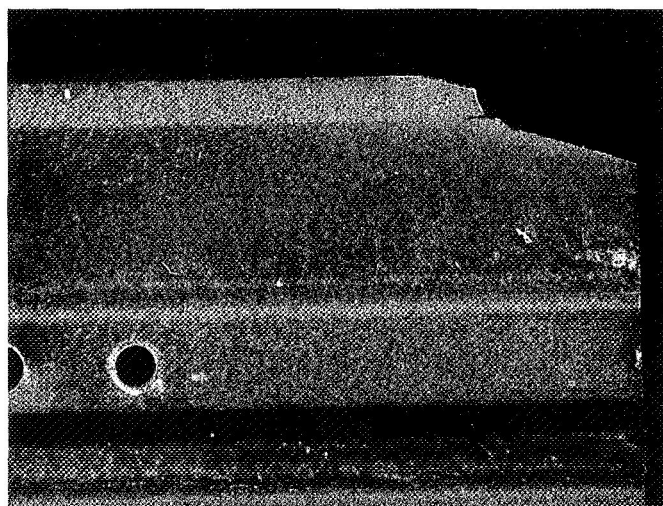


Fig. 19. Failed female shutter blade (part 1)



**Table 5. Description of failed parts**

Failure data	Part 1	Part 2
	Failure of 1-21-70	Failure of 2-2-70
Shutter unit	Engineering model	Engineering model
Shutter driver at time of failure	MM'71 test set	MM'71 test set
Test temperature at time of failure	-50°C	-50°C
Number of test cycles		
On MM'69 driver	2,000	55,000
On MM'71 test set	10,913	3,087
Total	12,913	58,087
Description	Fracture of lip on female blade	Fracture of lip on male blade

**Table 6. Failure analyses**

Item	Test	Results
Identification of alloy	X-Ray diffraction (XRD-4 spectrometer)	Determined to be Type 1100 as required
Grain direction	Micro examination of etched sample	Grain normal to bend radii as required
Cracks in radii of aluminum or Al <sub>2</sub> O <sub>3</sub> (anodize)	Penetrant inspected	No cracks observed in aluminum or Al <sub>2</sub> O <sub>3</sub>
Thickness of aluminum and anodize	Mounted, sectioned, and measured thickness on photomicrographs	Aluminum: 0.0019-0.0023 in. Anodize: 0.0003-0.0004 in.
Maximum stress in shutter blade at -50°C	Stress analysis	10,000-psi (based on 0.0026 in. aluminum and 0.0006-in. anodize)
Fatigue strength of Type 1100-H14 aluminum at -50°C	Cryogenic Materials Data Handbook	Fatigue strength of Type 1100 aluminum greater at -50°C than at RT
Stability of shutter blades at low temperature	Expose to -50°C and measure deflection	Total distortion of 1/16-in. due to differential contraction between aluminum and Al <sub>2</sub> O <sub>3</sub>
Examined sections of failed shutter blades	Scanning electron microscope	Fatigue failures

(4) The fatigue strength of Type 1100 aluminum is greater at -50°C than at room temperature. The failure was not due to the properties of Type 1100 aluminum at -50°C.

(5) Failures were due to fatigue. The fatigue failures were initiated at -50°C by the high stresses caused by differential thermal contraction between aluminum and aluminum oxide, vibration of the shutter blades during operation, and scraping of the shutter blades caused by their distortion as a result of the differential thermal contraction.

*b. Materials, process, and design changes.* Recommended materials, process, and design changes were incorporated in new drawings. Each significant fact relating materials and processes to the design were examined in detail, and those items that could be improved without significant effect on schedule or cost were incorporated. The major required change, based on the analyses, was a change of the basic shutter material from 0.003-in.-thick Type 1100-H14 aluminum to 0.005-in.-thick Type 5052-H19 aluminum alloy. The other changes provided improved reliability and performance without significantly affecting schedule or cost. The materials, process, and design changes are summarized as follows:

Type 5052-H19 aluminum alloy per Federal Specification QQ-A-250/8, 0.005-in. thick, was selected to replace the previously used 0.003-in.-thick Type 1100-H14 aluminum. The reasons for selection of this available material were:

- (1) Higher satisfactory tensile and fatigue endurance limits. Compared with Type 1100-H14, tensile yield and ultimate are more than doubled, and fatigue endurance limit is almost tripled.
- (2) Deflection is indirectly proportional to the third power of thickness. The deflection of shutter blades at -50°C due to differential thermal contraction would be reduced considerably. As a first approximation (neglecting anodize thickness) deflection of the 0.005-in.-thick material would be about 0.013 in. This is considerably less than the designed clearance between mating shutter blades.

The bend radii requirement was changed from 0.020 to 0.025 in. to reduce probability of crack initiation during forming. Samples formed on production tooling and

first production parts were penetrant-inspected, and no cracks were observed.

The anodizing time was reduced from 60 to 30 min. This change reduced the thickness of  $\text{Al}_2\text{O}_3$  while maximizing the remaining thickness of aluminum alloy. The 30-min anodize met the solar reflectance requirements, as shown in Table 7.

The double-lip assembly on the female shutter blade was adhesive-bonded in addition to riveting. Adhesive bonding is advantageous because of improved stress distribution. Epon 934 was selected because of its extremely low outgassing properties (essential because of the vicinity of critical optics) and semi-rigidity.

**c. Performance of new design.** No new problems appeared during manufacture of the new design. Forming, anodizing, adhesive bonding, riveting, and other manufacturing operations have been free of incidents or problems.

50,000 test cycles on one pair of experimental shutters have been performed at room temperature without failure. 8000 test cycles, including approximately 2000 cycles at  $-50^\circ\text{C}$ , have been successfully accomplished on each of three pairs of flight shutters.

**Table 7. Results of solar reflectance measurements (measured at 0.4 to 0.76  $\mu\text{m}$ )**

Anodizing time, min	Solar reflectance	
	Measured, %	Specification 502703 requirement, %
30	0.058	$0.05 \pm 0.02$
50	0.045	$0.05 \pm 0.02$

### 3. Spacecraft Flight Loads Analysis

MM'71 flight-induced adapter loads (shear and moment at the spacecraft field joint) have been estimated using the acceleration time histories of the flight data recorded during the *Atlas-Centaur* (AC) flights of two MM'69 (AC-19, AC-20) one *Orbiting Astronomical Observatory* (OAO) (AC-16), and one *Applications Technology Satellite* (ATS) space vehicle (AC-17) (Fig. 20). To simplify the analysis, it was assumed that the six components of acceleration measured at the field joint

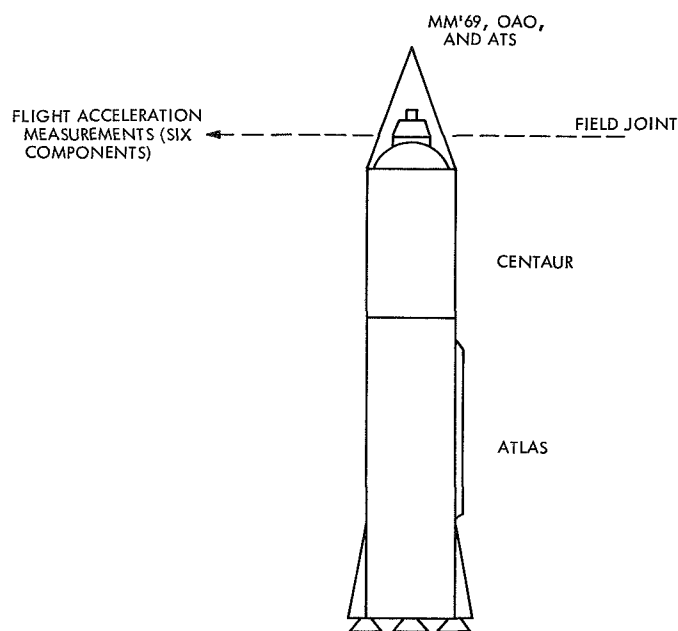


**Fig. 20. Flight acceleration measurement, *Atlas-Centaur* launch vehicle**

during the flight of MM'69, OAO, and ATS was relatively unaffected by the weight of the spacecraft. This assumption is warranted for the early part of the flight when the booster and the second stage represent the major part of the total vehicle weight. However, this assumption is less valid near the end of the flight, when the *Atlas* has been jettisoned and the *Centaur* is almost depleted of propellant.

A solution was found for the problem of determining the transient-type inertia loads at the field joint (Fig. 21), assuming that the MM'71 spacecraft would have been riding on the booster used for the two MM'69 spacecraft, the OAO, and the ATS.

The method analysis consisted of driving a mathematical model of the MM'71 spacecraft with the flight data to determine the required inertia loads. The measured flight data, in the form of acceleration time histories, were available on magnetic tape in an analog form for the total duration of the four boosted flights. The mathematical model used for the MM'71 spacecraft was represented by twelve normal modes of the spacecraft in a cantilevered configuration. Six of these normal modes had been measured during a modal survey conducted on the actual development test model (DTM) hardware. Six additional modes were mathematically added to represent four fluid slosh modes of the propellants in their

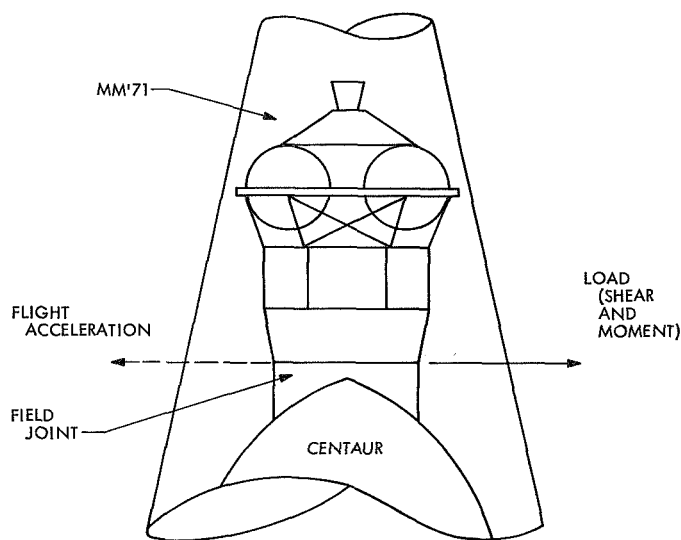


**Fig. 21. Mariner Mars 1971 load determination by simulation**

tanks and two solar panel modes. The damping for the spacecraft model was obtained by matching response acceleration of the tanks on the analog simulator with the actual response measured during the DTM forced vibration test. Once the twelve normal modes were patched on the analog computer, then this structural simulator is essentially an electronic black box having six inputs and four outputs (Fig. 22) and representing the dynamic structural characteristics of the MM'71 spacecraft in the frequency range of interest, i.e., below 60 Hz.

The six-channel flight data tape was then connected to the six inputs of the analog to simulate the flight accelerations that would have occurred to the MM'71 spacecraft if it had been riding on the specific flight investigated. The four outputs of the simulator were arranged to give the load time histories, i.e., the two components of shear force and the two components of moment about two axes in the plane of the field joint.

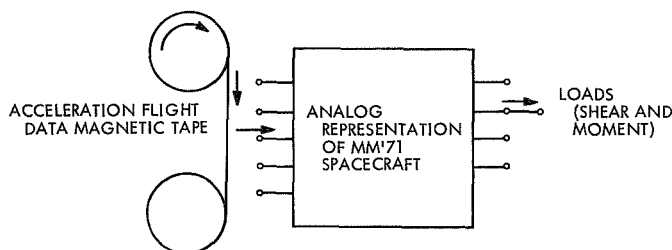


**Fig. 22. Analog determination of the adapter loads**

Those loads were recorded on O-graph for all the significant discrete events of the four flights, from booster ignition to spacecraft separation. The data is transient in nature, and the maximum peak load obtained from any time histories during one flight was selected. This maximum peak load occurred for the *Centaur* insulation panel jettison event for the four flights. Table 8 shows the value of those peak loads.

**Table 8. Adapter loads for insulation panel jettison**

Flight	Spacecraft weight, lb	Shear, lb	Moment, in.-lb $\times 10^3$
AC-16 (OAO)	4400	3700	290
AC-17 (ATS)	1750	5100	330
AC-19 (MM'69)	850	9800	620
AC-20 (MM'69)	850	5200	365
MM'71 spacecraft weight is 2100 lb.			

The AC-19 flight gave an abnormally high load which was rejected after careful evaluation of the data. The main criteria for rejecting the data was a substantial amount of electronic saturation that occurred for two channels of telemetry during the event. Other considerations were also investigated, such as a possible mechanism to produce such a high peak in the raw data. No reasonable mechanism was found.

It is worth noting that the loads of Table 8, excluding AC-19, exhibit a trend in terms of the weight of the spacecraft showing that the original assumption is only partially true. This trend was accounted for, using a least-square best-fit technique. Table 9 shows the resulting mean and  $3\sigma$  value of the estimated MM'71 flight loads. These estimated flight loads are smaller than the structural design criteria loads shown in Table 9.

**Table 9. Statistical values of the MM'71 field joint loads (loads analysis results versus design criteria)**

Measurement	Mean	$3\sigma$ value	Design criteria
Shear, lb	4750	5224	9000
Moment, in.-lb $\times 10^3$	325	377	450

## F. Propulsion

### 1. Pressurant Relief Assembly Studies

*a. Introduction.* The *Mariner* Mars 1971 propulsion subsystem uses nitrogen gas pressurization for both fuel and oxidizer propellant tanks. Each propellant tank has a pressurant relief valve which terminates in a tee with two opposed nozzles. The relief valve vents pressurant gas if pressures reach 290 to 330 psid. Unbalanced torque produced on the spacecraft during venting is minimized by selective pairing of nozzles. Unbalanced forces can also be induced on the spacecraft due to impingement of the vent nozzle plumes on the thermal blanket which is asymmetrical with respect to the vent tee assembly. Figure 23 shows the location of the vent noz-

zles with respect to the thermal blanket and Canopus sensor. Although the vent nozzle plumes do not directly impinge on the Canopus sensor, it is necessary to determine if any increase in pressure at the Canopus sensor occurs during venting. This is important, since pressures of the order of  $2.0 \times 10^{-6}$  psia can support an arc/corona discharge within the Canopus sensor.

Two of the above-mentioned problems have been studied and are reported here. An analysis of the deflected flow from the thermal blanket has been completed, and an estimate has been made of the increase in pressure at the Canopus sensor. Two pressurant relief valve vent nozzles have been flow-tested to determine the maximum unbalanced thrust produced when the

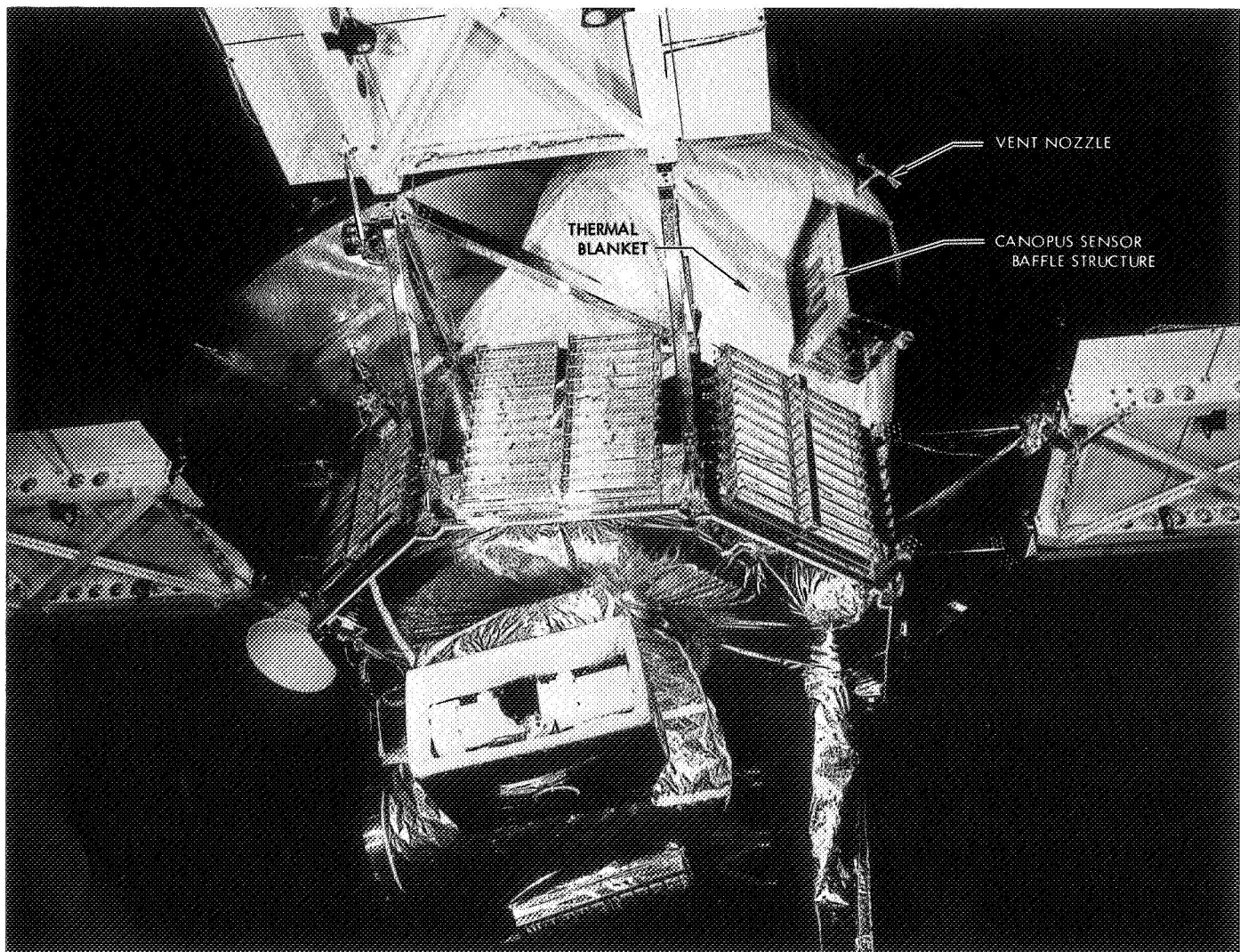


Fig. 23. Relationship of relief valve vent assembly to thermal blanket and Canopus sensor

nozzles are vented through a tee assembly. An analysis of the unbalanced torques produced by plume impingement on the thermal blanket will be made in the future.

**b. Canopus sensor impingement.** Although the vent nozzle plumes do not directly impinge on the Canopus sensor, they do impinge on the spacecraft thermal blanket, creating deflected flows which can reach the outside of the Canopus sensor shroud. Since pressures of the order of  $2.0 \times 10^{-6}$  psia can support an arc/corona discharge if they occur within the Canopus sensor<sup>3</sup> it is necessary to determine if pressures of this magnitude can be generated by the deflected flows. Although a method of characteristics (MOC) solution for the vent nozzle plume was available for one flow rate and stagnation pressure, it was decided to approximate the plume by a simpler method which would allow easier variation of parameters. The method used for plume flow field definition is discussed in the following section.

**c. Plume flow field definition.** The approximate plume flow field used is based on the method of Hill and Draper (Ref. 1). The method assumes that for the far field, the flow is radial from a point source and that the velocity has reached the maximum exhaust velocity given by

$$V_m = \sqrt{\frac{2 g_c \gamma R T_0}{\gamma - 1}} \quad (1)$$

From consideration of many exact solutions (MOC) of plume flow fields, the mass distribution in the plume is approximated by

$$\left(\frac{d\dot{m}}{d\Omega}\right)_\theta = \left(\frac{d\dot{m}}{d\Omega}\right)_{\theta=0} \exp[-\lambda^2 (1 - \cos \theta)^2] \quad (2)$$

where

$$\lambda = \frac{1}{\sqrt{\pi} \left(1 - \frac{C_F}{C_{F_{\max}}}\right)} \quad (3)$$

$$\left(\frac{d\dot{m}}{d\Omega}\right)_{\theta=0} = \frac{\dot{m}\lambda}{\pi^{3/2}} \quad (4)$$

<sup>3</sup>Swenson, D., *Mariner VII Anomaly—Electrical Discharge*, Nov. 10, 1969 (JPL internal document).

From the radial flow assumption, the mass flow per unit solid angle can also be expressed as

$$\left(\frac{d\dot{m}}{d\Omega}\right)_\theta = \rho V r^2 \quad (5)$$

Combining Eqs. (2) and (5) and considering the maximum venting flow rate case (0.125 lbm/s and 56 lbf/in.<sup>2</sup> stagnation pressure), the equation for the lines of constant density in the plume is

$$r^2 = \frac{1.422 \times 10^{-4}}{\frac{\rho}{\rho_0}} \exp[-73.05 (1 - \cos \theta)^2] \quad (6)$$

Constant density contours for this case are given in Fig. 24. Results from this approximate method and the available MOC solution gave good agreement in the far field region.

**d. Impingement pressures on thermal blanket.** Calculation of impingement pressures is complicated by the complex shape of the spacecraft thermal blanket. An approximate shape for the thermal blanket was obtained by carefully examining a mock-up of the thermal blanket and looking at drawings of the spacecraft structure. The plume/thermal blanket intersection was considered in a plane containing the vent nozzle axis and the Canopus sensor. This plume/thermal blanket intersection was then superimposed on the plume flow field solution of Fig. 24.

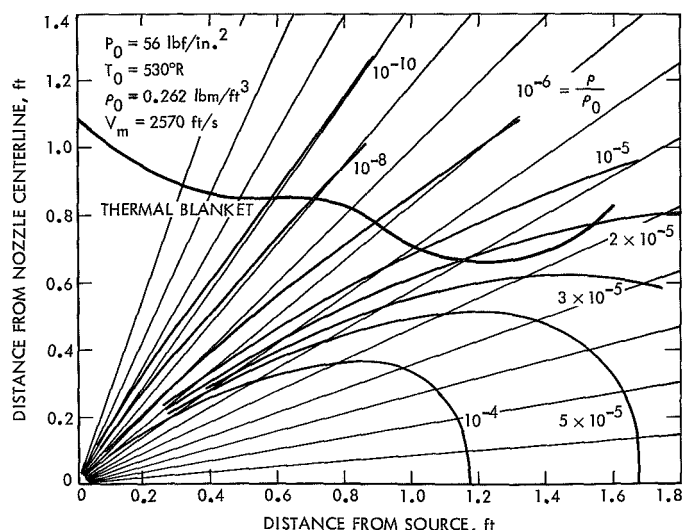


Fig. 24. Vent nozzle plume density contours

Impingement pressures were calculated by a method similar to that of Maddox (Ref. 2). At each intersection of a constant density contour with the thermal blanket surface, the impingement pressure was calculated using

$$P = \rho V^2 \cos^2 \theta_N \quad (7)$$

where

$$V = V_m \text{ (far-field approximation)}$$

$$\theta_N = \text{angle between velocity vector and surface normal}$$

A pseudo-stagnation point is assumed to exist at the point on the surface where  $\rho V^2 \cos^2 \theta_N$  attains a maximum. The flow upstream of this stagnation point is assumed to have insufficient momentum to overcome the pressure gradient.

**e. Deflected flow.** A deflected flow is assumed to originate at the pseudo-stagnation point and expand isentropically under the influence of the pressure gradient imposed on the thermal blanket by the vent nozzle plume. Once outside the plume, the deflected flow is assumed to undergo a cylindrical expansion to the Canopus sensor location. The maximum impingement pressure on the Canopus sensor, using the Newtonian approximation, was calculated to be  $3.0 \times 10^{-6}$  lbf/in.<sup>2</sup> Since this pressure appears to be above the pressure required to support an arc/corona discharge in the Canopus sensor (Footnote 3), the deflected flow could lead to a problem if relief valve venting occurs, unless the Canopus sensor is adequately protected from this pressure environment. Although the above pressures were calculated for the maximum venting flow rate, calculations show that pressures of the same order would be generated for a nominal venting flow rate.

Initially, the spacecraft thermal blanket was secured around the Canopus sensor structure with a slip-string fastener. As a result of the above analysis, which predicts a potential problem, the Canopus sensor/thermal blanket interface will now be sealed with tape to prevent any pressure buildup within the Canopus sensor during venting of the pressurant gas.

**f. Vent nozzle test.** The twelve vent nozzles to be used on three spacecraft have been measured and found to have throat diameters from 0.2499 to 0.2515 in. The nozzles were matched in pairs to minimize the geometrical mismatch of any two nozzles operating from the same

vent tee. A flow test has been made using the most geometrically mismatched vent nozzle pair (SN 004 with throat diameter of 0.2509 in. and SN 007 with throat diameter of 0.2515 in.) to determine the maximum unbalanced thrust.

A sketch of the test setup is shown in Fig. 25. A tee with dimensions equal to those of a flight tee was fabricated from aluminum stock. The tee had a 14-in.-long entrance tube made of 0.5-in. OD 20-gauge aluminum tubing. The entrance tube was rigidly mounted to a 3- × 4-in. aluminum angle 12 in. upstream of the tee. Four silicon semiconductor strain gauges were connected in a Wheatstone bridge circuit and mounted on the entrance tube 10 in. upstream of the tee with EPY-150 cement. To obtain bridge balance, a 3.3 kΩ resistance was added in parallel with one of the gauges. This led to temperature drift problems during the test due to a lack of temperature compensation in the bridge circuit. The strain gauge output was recorded on both a Moseley strip chart recorder and an oscillograph.

The tee assembly was rigidly mounted to a wall with the entrance tube vertical and the nozzles venting horizontally. The test was conducted at atmospheric pressure using room temperature nitrogen gas. Flow rates were measured with a calibrated thin-plate orifice, and the orifice pressure drop was recorded on a Moseley strip chart recorder. Static pressure was measured in the entrance tube 14 in. upstream of the tee.

It was necessary to add a viscous damper to the tee assembly to prevent large amplitude vibrations at the

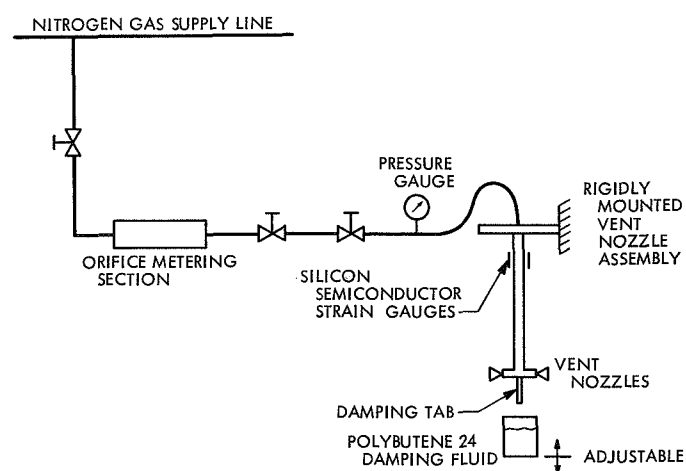


Fig. 25. Vent nozzle test setup

natural frequency of the tee assembly, which was approximately 50 Hz. The damper consisted of a 1- × 3-in. aluminum tab immersed in a container of polybutene 24. The amount of viscous damping was adjusted to obtain a slightly overdamped system.

The test covered a range of flow rates from 0.06 to 0.125 lbm/s. The measured nozzle thrust mismatch was about 0.25 oz for the maximum flow rate condition with the SN 007 nozzle giving the higher thrust. This is compared with a 0.19-oz predicted thrust mismatch for the maximum flow rate condition in the atmospheric test. Assuming the ratio of thrust mismatch to thrust remains constant, an extension of these results to the vacuum expansion case indicates that nozzle thrust mismatch should not exceed 0.5 oz, which corresponds to an unbalanced spacecraft torque of 1.15 in.-lbf, well within the 2.0 in.-lbf capability of the attitude control system. The nozzle thrust mismatch of the other pairs of vent nozzles should be less than the measured values, since their geometrical differences are much less than the nozzle pair tested.

Superimposed on the measured thrust mismatch was a random fluctuating  $\pm 0.5$ -oz thrust component, which was probably caused by nozzle separation effects in this atmospheric test.

In addition to the unbalanced torque produced by slight differences in nozzle geometry, the effects of plume impingement on the asymmetric thermal blanket must be included to determine the probable total unbalanced torque due to venting in flight. Plume impingement effects will be calculated using a method-of-characteristics loads program.

### References

1. Hill, J. A. F., and Draper, J. S., "Analytical Approximation for the Flow From a Nozzle Into a Vacuum," *J. Spacecraft*, Vol. 3, No. 10, pp. 1552-1554, Oct. 1966.
2. Maddox, A. R., "Impingement of Underexpanded Plumes on Adjacent Surfaces," *J. Spacecraft*, Vol. 5, No. 6, pp. 718-724, June 1968.

## II. Viking Project, Orbiter System and Project Support

### A. Project Description and Status

#### 1. Description

The primary objective of the *Viking* Project is to send two vehicles to the planet Mars to perform scientific experiments directed toward enhancing current knowledge about the physical characteristics of the planet, particularly its capability for supporting life and possible evidence of life. The two vehicles, each consisting of an orbiter system and a lander system, are anticipated for launch during 1975. The orbiter system will be developed by JPL, and the lander system will be developed by the Martin-Marietta Corp. Langley Research Center has overall management responsibility for the *Viking* Project.

The orbiter system will transport and inject the lander system at the appropriate point for a selected landing site and will relay telemetered data from the lander to earth. Scientific instruments on the orbiter will be used to measure atmospheric and surface parameters at various times and locations to determine the dynamic characteristics of the planet. The topography of Mars will be

mapped during orbital operations, with special emphasis on mapping the proposed landing site prior to deorbit of the lander system and on supporting the lander after it is on the surface of Mars by determining if changes are apparent in the vicinity of the lander. Both visual and infrared coverage will be possible during the presently planned 140 days of orbital operations.

During entry and after landing, the scientific instruments on the lander will measure Mars' atmospheric composition, temperature, pressure, and density. After landing, the topography of the landing site will be mapped, and measurements will be made of the planet's surface composition, temperature, pressure, humidity, and wind speed. Of particular interest in the surface measurements are the type of organic compounds present, if any, and the amount and form of water. A gas chromatograph/mass spectrometer, for measuring both atmospheric and surface composition, is being developed by JPL. The surface soil analyses will be directed at detecting evidence of growth and/or metabolism.



## 2. Status

JPL's cost estimates for the reprogrammed *Viking* orbiter 1975 activities were presented to the Project Office at Langley Research Center and were followed by an on-site review of cost backup data at JPL.

Work is essentially completed on commonality studies between the Venus-Mercury 1973 and the *Viking* orbiter 1975 missions. However, the changes in implementation modes that are necessary to achieve the savings possible through commonality, plus the requirement for early commitment of resources and design requirements, may make commonality difficult to utilize. Additional review effort is currently aimed at determining if some subsystems should be acquired in a common arrangement, with benefit to both projects.

## B. Guidance and Control

### 1. Automatic Sun Occultation—Sun Acquisition Control for the *Viking* Spacecraft

*a. Introduction.* The *Viking* spacecraft orbital trajectory is such that the planet will pass between the spacecraft and the sun once each orbit during part of the orbital phase of the mission. The time duration of the sun occultation will extend from a few minutes to as much as 2 h, and to maintain attitude control during this period, the gyros will control the spacecraft in the inertial mode of operation. A proposed method to achieve this mode of operation is to detect occultation through the use of the sun gate in conjunction with the acquisition and cruise sun sensors. A signal from these sensors will be used to initiate inertial control of the spacecraft.

*b. Mechanization.* Automatic sun occultation control would be performed on the *Viking* spacecraft by detecting the difference between the sun occultation mode and the sun acquisition mode. This information would then be used to place the gyros either in rate mode (sun acquisition) or in inertial mode (sun occultation). This mechanization works in the following manner for sun occultation: As the spacecraft begins sun occultation, the dark threshold of the sun gate is exceeded. This causes the sun gate electronics to change state, which turns on the gyros. At the same time, the sun sensors are being monitored by a level detect amplifier. Since there is no sun in the field of view of the sensors and the dark output impedance of the sun sensors is extremely high ( $>20\text{ M}\Omega$ ), the output will be at null. This information is used by the sun sensor level detect amplifier to put

the gyros in the inertial mode. The gyros stay in inertial hold until the sun reappears in the sun gate field of view after sun occultation. At this time, the gyros will be turned off and the spacecraft returned to celestial control (sun and Canopus).

This method of occultation control has the advantage that it is automatic (requires no switching—no central computer and sequencer interface) and can always distinguish between sun acquisition and sun occultation.

For the sun acquisition mode, this mechanization detects the loss of the sun gate and when the sun is in the field of view of either the acquisition sun sensors or the cruise sensors. The voltage errors out of the sensors are continuously monitored. When the angle between the  $-Z$  axis and the sun is greater than 2 deg, the level detect amplifier then commands the gyros to rate mode for automatic sun acquisition.

The logic for sun occultation/sun acquisition is as follows:

- (1) *Sun occultation.* Loss of sun gate plus sun sensors at null will turn on the gyros in the inertial mode and the spacecraft will stay inertially controlled during the sun occultation period.
- (2) *Sun acquisition.* Loss of sun gate plus sun sensors error not at null will turn on the gyros in the rate mode and the spacecraft will automatically acquire the sun.

A functional block diagram of the sun occultation/sun acquisition logic is shown in Fig. 1.

*c. Sun sensor characteristics.* There are three types of sun sensors on the *Viking* spacecraft: the sun gate, the acquisition sensors, and the cruise sensors. To mechanize the automatic sun occultation/sun acquisition modes of spacecraft operation, all three sensors are used. The following descriptions of sensor parameters detail the behavior of the sensors in the sun occultation/sun acquisition environment.

*Sun gate.* In the sun occultation/sun acquisition mechanization, the sun gate will be required to operate in two different modes: (1) to sense the diminishing light intensity of the sun as the sun goes from partial eclipse to total eclipse (occultation mode), and (2) to sense if the angular error between the sun and the  $-Z$  axis of

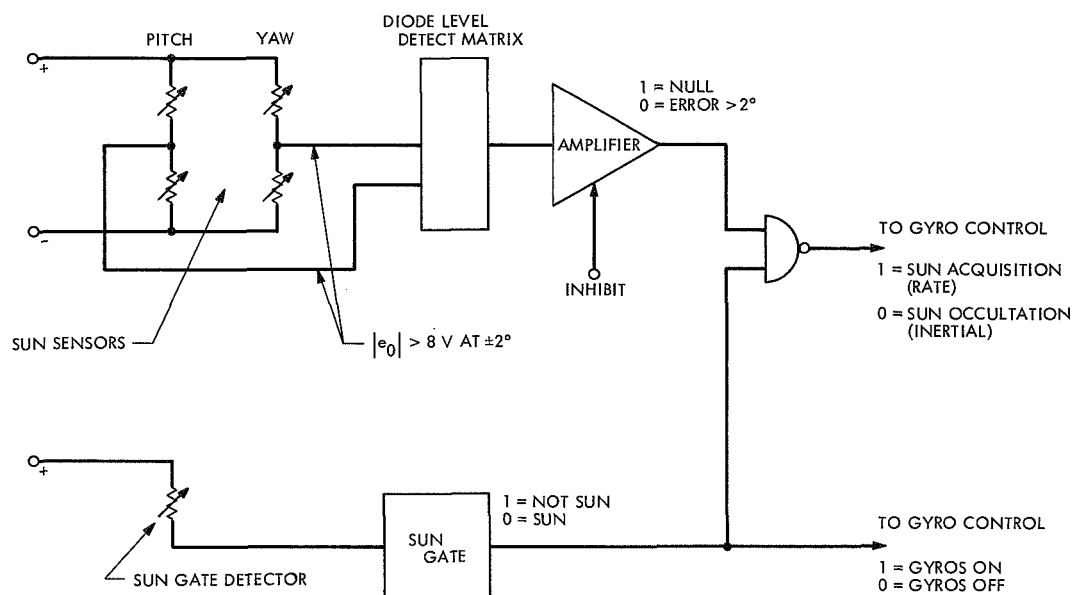


**Fig. 1. Viking sun occultation/sun acquisition mechanization**

the spacecraft is greater or less than 4.5 deg (acquisition mode).

Table 1 shows the sun gate parameters at Mars (redundant sun gate detectors). It can be seen that the sun gate will not detect sun occultation until the sun intensity has decreased from 5500 (full sun at Mars) to 288 ft-cd (dark threshold of sun gate). This means that sun eclipse will be ~95% complete when the sun gate changes state and turns on the gyros for spacecraft inertial control. Also, the sun gate acquisition threshold is approximately double the dark threshold. This means that the spacecraft will reacquire the sun (after occultation) when ~10% of the sun's surface area is exposed to the sun gate.

*Acquisition sun sensors.* These sensors cover the full spherical field of view of the spacecraft. The sensors

are arranged in a bridge configuration electrically and are shadowed mechanically such that one light sensitive cell is fully illuminated and one is totally dark during sun acquisition (Fig. 2). The characteristics of the sensor around null are very important for the sun occultation mechanization. Since the outputs of the acquisition sensors and the cruise sensors are summed in the level detect amplifier, it is important that the acquisition sensors are totally shadowed at null. The dark impedance of the acquisition sensors is greater than 20 MΩ. This allows the cruise sensors and the sun gate to be determining elements for the sun occultation mode.

*Cruise sun sensors.* Figure 3 shows the characteristics of the cruise sun sensors. These sensors have a limited field of view around the -Z axis of the spacecraft ( $\pm 20$  deg). The voltage scale factor of the cruise sun sensors near null is 5 V/deg. This means that the cruise sensor is voltage-saturated at  $\pm 2\frac{1}{2}$  deg from null. This voltage is input to the level detect amplifier and is then used, along with the sun gate signal, to determine the sun acquisition mode. (Gyros are ON in the rate mode.)

**Table 1. Sun gate parameters at Mars**

Occultation mode		
Threshold	Light intensity, ft-cd	Resistance, KΩ
Acquisition	546	13
Dark	288	18
Acquisition mode		
Threshold	Sun angle, deg	Resistance, KΩ
Acquisition	4.5	13
Dark	4.75	18

An important characteristic of the cruise sun sensors during the period from the start of sun eclipse to sun occultation is the ability of the sensors to track the sun accurately as the sun intensity and size diminish. Tests show the null offset errors to be less than  $\frac{1}{2}$  deg, while the sun intensity was reduced from 12,000 to 30 ft-cd. Since the minimum intensity of the sun at the

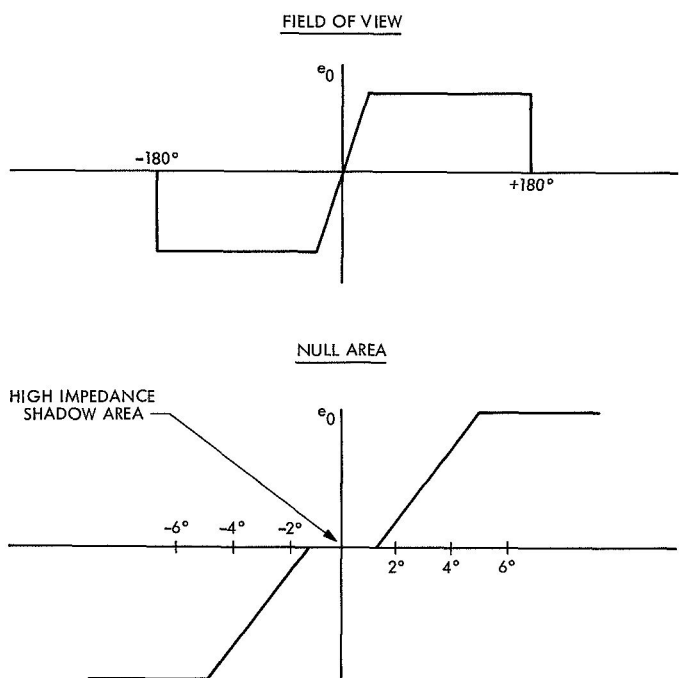
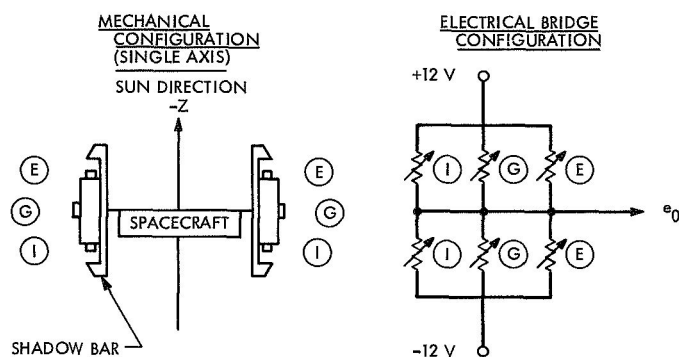


Fig. 2. Acquisition sun sensor

moment of occultation sensing is approximately 300 ft-cd, the sensors are expected to track the sun without significant spacecraft position error.

**d. Gyro "inertial start" requirements and performance.** A computer program has been generated to show the effects of gyro performance on the spacecraft during the "inertial start" mode of operation. This program uses worst-case start-up transient models in an effort to determine if the spacecraft can accurately maintain its inertial position during the critical gyro spin-motor run-up phase. The results of the computer runs are shown in Figs. 4, 5, and 6.

The graphs show two curves—actual position and pseudoposition. These curves represent spacecraft posi-

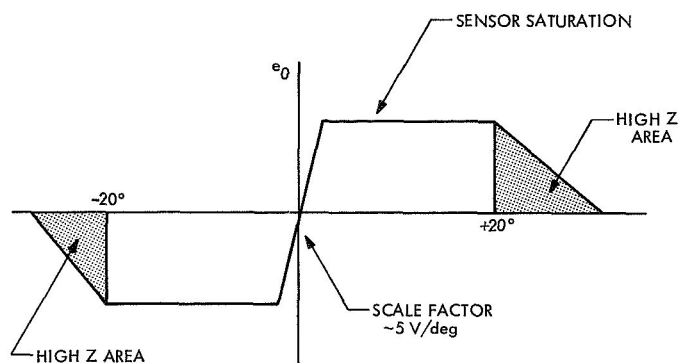


Fig. 3. Cruise sun sensor electrical parameters

tion and gyro integrator position. Input to the program is the gyro rate hang-off during spin-motor run up (4 deg/h), a model of the gyro transfer function versus time, and the gyro spin-motor run-up time. Figures 4, 5, and 6 show the spacecraft behavior for gyro spin-motor run-up times of 1, 3, and 5 min. Typical gyro run-up times at room temperature or above are 60 s or less. The following table summarizes the results:

Run-up time, s	Spacecraft position, deg	Integrator position, deg
60	0.00	0.07
180	0.36	0.08
300	0.71	0.08

Even in the unlikely case of an extremely long gyro run-up, the spacecraft position is held to less than 1 deg. These position errors are small and do not in any way impair the ability of the spacecraft to reacquire celestial references (sun and Canopus) after sun occultation.

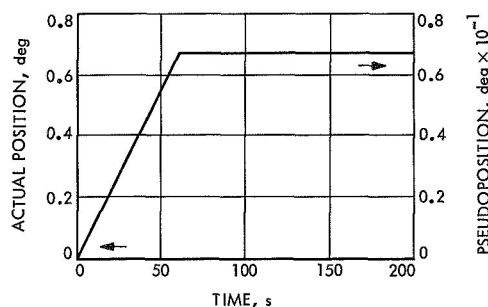


Fig. 4. Actual position and pseudoposition vs time (for 1-min gyro run-up time)

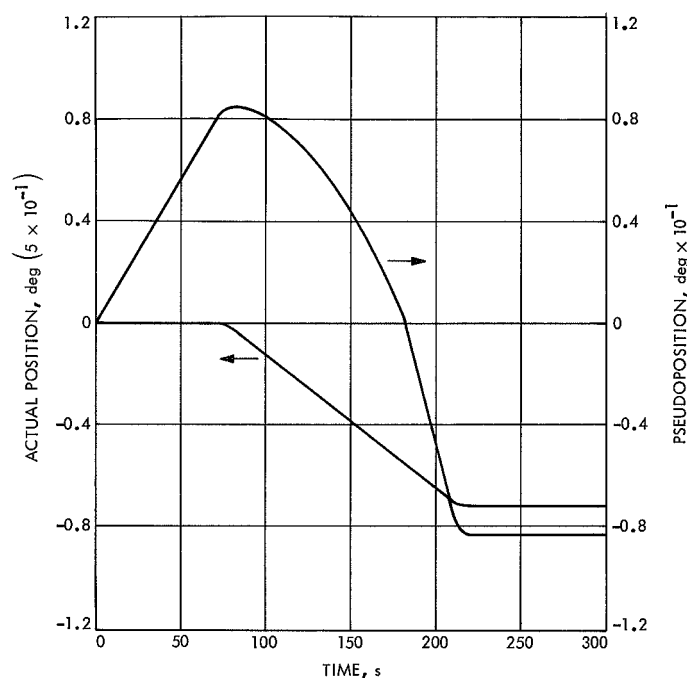


Fig. 5. Actual position and pseudoposition vs time (for 3-min gyro run-up time)

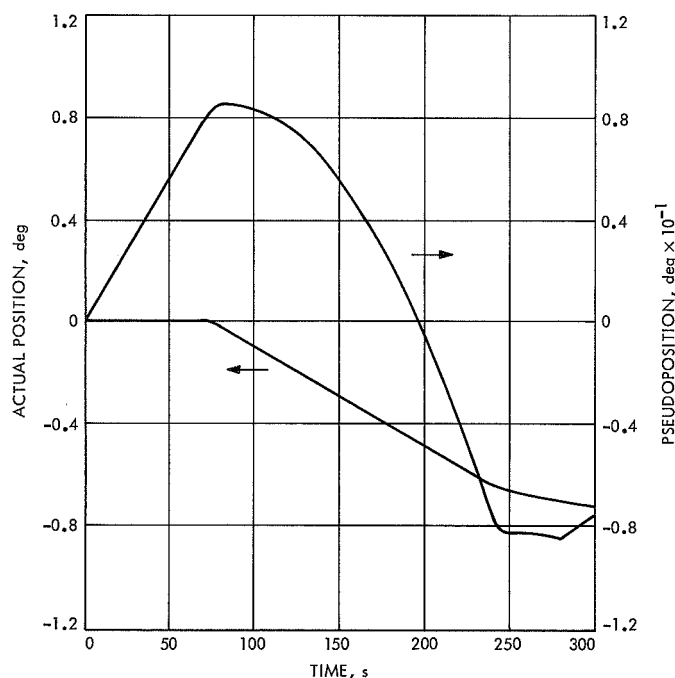


Fig. 6. Actual position and pseudoposition vs time (for 5-min gyro run-up time)

**e. Orbital considerations.** The sun occultation periods vary in length as the orbital mission progresses. Also, the time between start of eclipse to full eclipse varies

as a function of spacecraft velocity and distance from the planet. Two representative sun occultation periods are listed below:

Parameter	Case 1	Case 2
Distance from planet, km	4,000	20,000
Time after periapsis, min	30	240
Partial eclipse time, s	20	178
Total occultation, min	70	120

**f. Conclusions.** This article describes the parameters that are relevant to the automatic sun occultation/sun acquisition mode of spacecraft control. This concept is moderately simple to mechanize and has the unique advantage of always being able to detect the difference between the sun occultation mode and the sun acquisition mode.

## C. Engineering Mechanics

### 1. Thermal Design

**a. Introduction.** Temperature control of the *Viking* orbiter consists of both the design and development of the hardware items, such as louvers, blankets, heaters, etc., and the effective use of these tools to achieve an acceptable overall or system thermal design. This article discusses the thermal design of the *Viking* orbiter from the point of view of the entire system heat balance; this thermal design will later form the basis for the detail design of specific parts of the spacecraft.

**b. Temperature control.** From a temperature control viewpoint, the *Viking* orbiter (Fig. 7) is composed of three major thermal assemblies plus appendage equipment. The three major elements are: (1) the bus that houses most of the electronic subsystems; (2) the mid-course and orbit insertion propulsion module that consists of tankage and the engine; and (3) the science scan platform that consists of a dual imaging subsystem (two TVs), an infrared thermal mapper, and a Mars atmospheric water detector. Appendage equipments are those items not contained within the three major assemblies, such as the antennas, solar panels, etc.

In relating *Viking* orbiter with past *Mariner* spacecraft, some striking thermal differences become evident. Physical size is the primary difference. The *Viking* spacecraft is considerably larger than the *Mariner* spacecraft, with

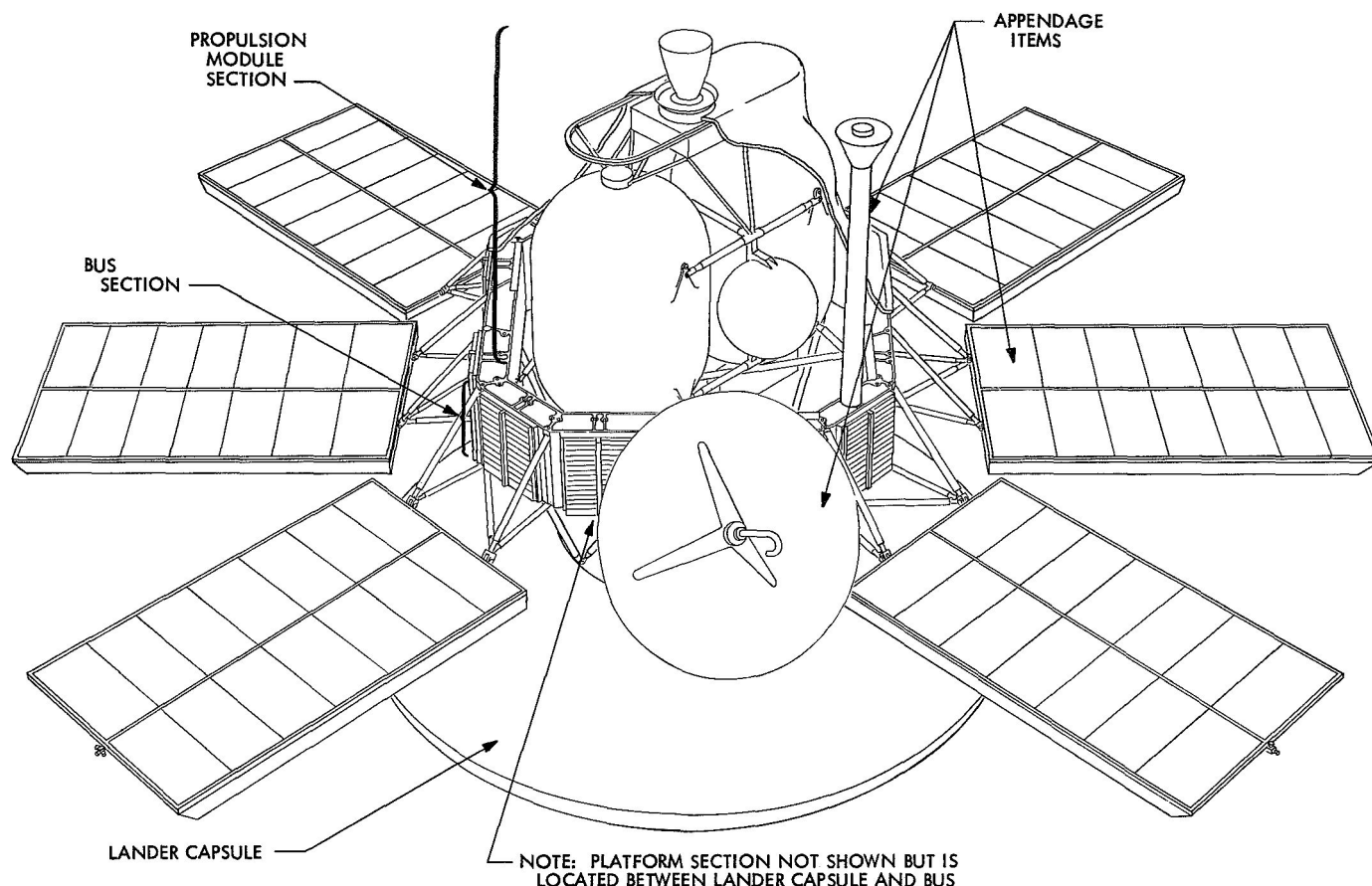


**Fig. 7. Viking orbiter simplified configuration**

external surface area being roughly three times that of the *Mariner* Mars 1969. On the other hand, internal power dissipation has increased only by a factor of two. Consequently, the conservation of internal power becomes relatively more important. The propulsion module has become much larger; consequently, its temperature control cannot be achieved by thermal coupling to the bus with perhaps a small amount of electrical heating, as was done in the past. The propulsion module must be treated as a separate thermal entity even though roughly one third of its tankage is nested within the bus cavity. This nesting does, in fact, cause a fair amount of coupling; however, because the bus cannot supply a sufficient amount of thermal energy to the propulsion module, the design approach is to negate the coupling by maintaining the propulsion module bulk temperature near that of the bus, creating on the average an adiabatic interface. Solar energy will be utilized to maintain propulsion module temperatures.

The scan platform is presently ill-defined in a specific thermal sense, since mission requirements are still under

study. In a general sense, the *Viking* scan platform is similar to past *Mariner* platforms, with a couple of exceptions. First, the thermal environment is somewhat different due to the large obstruction to viewing of space created by the *Viking* lander; and second, the complement of instruments are new, with perhaps tighter thermal constraints. Even with these differences, the temperature control design approach to the *Viking* platform remains essentially the same as for *Mariner* spacecraft.

Since very little thermal design has been done on appendage items, they will not be discussed here.

**c. Bus.** Other than the striking increase in size, the *Viking* orbiter bus is generally similar to those of past *Mariner* spacecraft. It appears that past techniques will be adequate and will offer a fair degree of design flexibility and operational reliability. These techniques are of either the passive or semi-active type and include painted and polished metal surfaces, multilayer insulation, electrical heaters, and louver arrays.

The *Viking* bus contains 16 equipment bays. Of the 16 bays, 12 contain electronic subassemblies, two contain the attitude control gas bottles, one contains the Canopus sensor, and one serves as a mounting platform for the high-gain antenna. The shape is an imperfect octagon with four sides that contain three bays each and four that contain one bay each. The bays form a ring that encloses about a third of the propulsion module. The central cavity is to be closed off on one end by a multi-layer blanket installed as a "drum skin" over the cavity to the outer periphery of the octagon. Out of the other end of the bus, the protruding propulsion module will also be blanketed, thus forming an enclosure that includes the bus cavity and propulsion module.

At present, four of the 12 bays that house electronic subsystems are nominally dormant during cruise. The temperatures of these four bays will be maintained by four 10-W substitution heaters. The four zero- or low-power bays that contain the attitude control gas bottles, Canopus tracker, and the high-gain antenna mount will be sandwiched between dissipating bays, thus obtaining thermal energy by conduction and radiation coupling.

Further details regarding power and power distribution within the bus are contained in SPS 37-62, Vol. I, pp. 35-43.

**d. Propulsion module.** Thermal efforts relative to the propulsion module concentrated on two problem areas: (1) maintaining the module warm during cruise and in Mars orbit, and (2) keeping various components within acceptable temperature limits during the long orbit insertion burn. Both of these problems are more severe for *Viking* 1975 than for the similar but smaller *Mariner* Mars 1971 spacecraft. Solution of the first problem is based on the use of a new development item, dubbed the solar energy controller (SEC). A feasibility model of the SEC has already been tested (SPS 37-62, Vol. I), and the first thermal flight prototype is currently being fabricated. Standard techniques, such as selective thermal coating, insulating, etc., hopefully will be sufficient for solving the soak-back heating that follows the orbit insertion burn.

**Solar energy controller.** Early calculations indicated that the temperature control of the propulsion module would require 20 to 30 W more electrical power than *Mariner* Mars 1971. This additional energy requirement results from a larger propulsion module (a larger radiating area), an assumed low thermal coupling with the bus,

and a minimum solar intensity at Mars aphelion (rather than the near perihelion condition for the *Mariner* Mars 1971 spacecraft). Obtaining 30 more watts by additional solar panel area would increase the spacecraft weight by at least 8 lb. For this same weight, 80 W can be provided to the propulsion module with four SEC units.

Briefly, the SEC is a shuttered greenhouse window. The greenhouse window is transparent to the solar energy allowed through the shutters and opaque to the infrared energy emitted from within the orbiter. For the flight model, the plane of the window is approximately in line with the sun. Articulated louvers normal to the sun regulate solar energy onto a highly reflective surface. The energy reflected from the surface passes through the window and is reflectively spread onto the propulsion tanks, structure, etc. By being independently controlled from the ground through the flight command subsystem, the SEC will not only maintain the propulsion module at a desired average temperature, but also minimize the thermal gradients expected in the propulsion module.

**Soak-back heating.** Except for the engine skirt, the *Mariner* Mars 1971 engine is the same as the *Viking* 1975 engine, and keeping cognizant of the *Mariner* Mars 1971 thermal control techniques has been the principal effort in this region of the propulsion module. Without a major modification, it is doubtful that any significant improvement can be made over the temperature control methods established by *Mariner* Mars 1971. For example, the addition of a louver system for dumping heat in the immediate vicinity of the engine or the development of a heat pipe arrangement to transport heat to the top of the propulsion module are possible, but not currently planned. Temperatures higher than those determined for *Mariner* Mars 1971 can be expected because of the significantly longer *Viking* 1975 orbit insertion burn.

Early calculations indicated the propellant tanks would reach a temperature locally higher than the design point of 90°F, due to the longer burn time. The *Mariner* Mars 1971 thermal control model test results have also confirmed that a temperature above 100°F should be expected. As soon as the 1971 test results become available, the propulsion analytical model will be refined and how much the local tank temperatures will rise above 100°F can be estimated. This design point has been tentatively increased to 120°F, and the mounting of the motor has been changed from that of a magnesium bridge to a lower conductive truss support.

*e. Scan platform.* The scan platform is composed of advanced new scientific instruments. The most thermally sensitive of these instruments are the Mars atmospheric water detector (MAWD) and the optics of the two TV telescopes. These instruments cannot tolerate temperature gradients of over 3°F across the longest dimension, and the absolute temperatures must be maintained to about the same degree of accuracy.

The scan platform internal thermal environment is stabilized by the application of 60 W of continuously applied electrical power. The 60-W value is preliminary and is based on the assumption that the total thermal power required for temperature control will not be significantly different than that required for past *Mariner* spacecraft. The 60 W will be derived from electrical heaters operated off the main regulated dc bus when the science instruments are off. For the science on condition, the 60 W will be derived from a combination of electronic dissipation and heater dissipation. The essential point is that a regulated 60 W will be dissipated and that this power will be dissipated in thermally identical locations (to the extent possible) regardless of whether the instruments are on or off.

The powering of all platform heaters from a regulated supply rather than off the unregulated supply is a new departure and derives from the desire to achieve a constant power input to the platform. The unregulated supply voltage can vary from 28 V to perhaps 50 V, depending upon mode (battery or solar panels) and solar panel temperatures. These large power variations lead to significant amounts of test time to establish design adequacy under all conditions and also may be in conflict with the temperature constraints. The regulated supply will eliminate some of these problems.

It is anticipated that all of the scan platform will be enclosed in a multilayer insulation blanket to conserve thermal power and thermally integrate the instruments. Also, the platform will be thermally isolated from the bus and sun. To compensate for uncertainties in insulation performance and to prevent a cascading effect should any single instrument fail, some type of variable emittance device will be utilized, probably a louver array.

Externally, the scan platform is influenced by the interaction of the backside of the solar panels, the bus interface, and the large biocanister of the *Viking* lander, which presents one effect when attached and another

effect when jettisoned. It is believed that the insulation blanket will tend to dampen these effects.

In Mars orbit, the planet influences the platform to a predictable but significant degree. All of the requirements and constraints for the scan platform are not yet entirely known; but the scan platform instruments, particularly the MAWD, must view wide areas of Mars to aid in the selection of an appropriate landing site.

The MAWD instrument is the most difficult instrument on the scan platform from a thermal control design standpoint since it must have not only low thermal gradients but a low (−100°F) temperature for the detector. This low temperature is provided by a thermal radiator plate, which is part of the MAWD, that views out from the scan platform blanket.

The performance of the MAWD radiator is influenced externally by all of the surfaces within view, which include the lander, bus interface, and solar panel backside. The view factors to these surfaces vary with both cone and clock angle of the scan platform, so many positions must be evaluated to determine the worst case. Also, conditions after the lander is jettisoned must also be considered as well as the transient thermal effects of the Mars infrared and reflected solar energy. The internal heat load to the MAWD detector consists of radiation from the instrument walls, thermal conduction through the detector mounting system, and the radiant flux received while viewing the planet.

The temperature control goals for the MAWD are dictated not only by the ambient temperature (70°F) and gradient requirements (3°F max) but, in addition, by the detector temperature level (−100°F) and the allowable transient temperature change rate (3°F/h). These temperature requirements are extreme and to achieve them a very careful heat balance will be necessary and, perhaps, new and unique thermal control devices will have to be considered.

## **2. Ground Handling and Assembly Equipment**

*a. Introduction.* Engineering mechanics effort for the *Viking* 1975 Project includes the design, fabrication, and, in many cases, the use of the mechanical ground handling and assembly equipment. Although many of these activities are still in the planning stage, the basic ground handling philosophy has been selected and general techniques have been outlined for the major activities. This article briefly discusses the ground handling

design approach, assembly and test sequences and equipment, and indicates departures from previous practices. Although handling of the entire *Viking* spacecraft is not JPL responsibility, combined operations which involve the orbiter and other major hardware items must be considered.

**b. Design approach.** The basic ground handling philosophy considers the operations at the Air Force Eastern Test Range as the most important. This does not detract from the importance of a well-designed ground handling system for the months of preflight testing, but emphasizes the need for a safe and reliable final assembly. To this end, the evolution of the basic equipment and procedures will begin in the early orbiter development tests and during the assembly and checkout of the proof test model and flight systems at JPL. For tests or operations which are planned for the orbiter development phases but are not part of the Cape Kennedy operations, the prime concern will be for the safety of the spacecraft and the operating personnel.

In past flight programs, the spacecraft was shipped to Cape Kennedy in an as completely assembled condition as possible because this method supported the various assemblies in the preferred way, reduced the number of containers and lost equipment, and reduced the packing and unpacking time. Shipments were made in standard-size electronic vans with approved suspension systems. Certain equipments, such as gyros, solar panels, batteries, etc., had peculiar characteristics and were handled separately. While this approach will still be followed where possible with the *Viking* orbiter, the large physical size of the assembled orbiter precludes using this technique directly.

The orbiter consists of logical groupings of equipment which have similar if not identical assembly and qualification sequences. These major groups are the bus equipment, the propulsion module, the adapters, solar panels, and possibly the science platform. Separately, these groups (as well as the ground equipment to handle them) can be transported in standard-size vans, and to that extent the shipments will be made as major assemblies.

The bus, adapters, and propulsion module must be assembled as a base for the mounting of the accessorial assemblies. These assemblies will at least include the solar panels and the thermal blankets but may include the high-gain antenna, the science instruments, the attitude-control gas systems, and some electronic equip-

ment. An attempt will be made during the detail design period to keep the number of items which require late assembly to a minimum.

**c. Assembly sequences.** The basic assembly procedure permits the easy replacement of the major groups (lander/capsule, propulsion module, and bus) in the event a quick change is necessary during final checkout or countdown. Also, the propulsion module and the bus electronics have significantly different pre-assembly checkout sequences (as is the case with the lander/capsule) and can be verified separately without imposing undue constraints on the other systems. By defining these criteria early in the design of the equipment, it is possible to have a greater influence on making the interface hardware durable and easy to assemble. This is true not only for the major

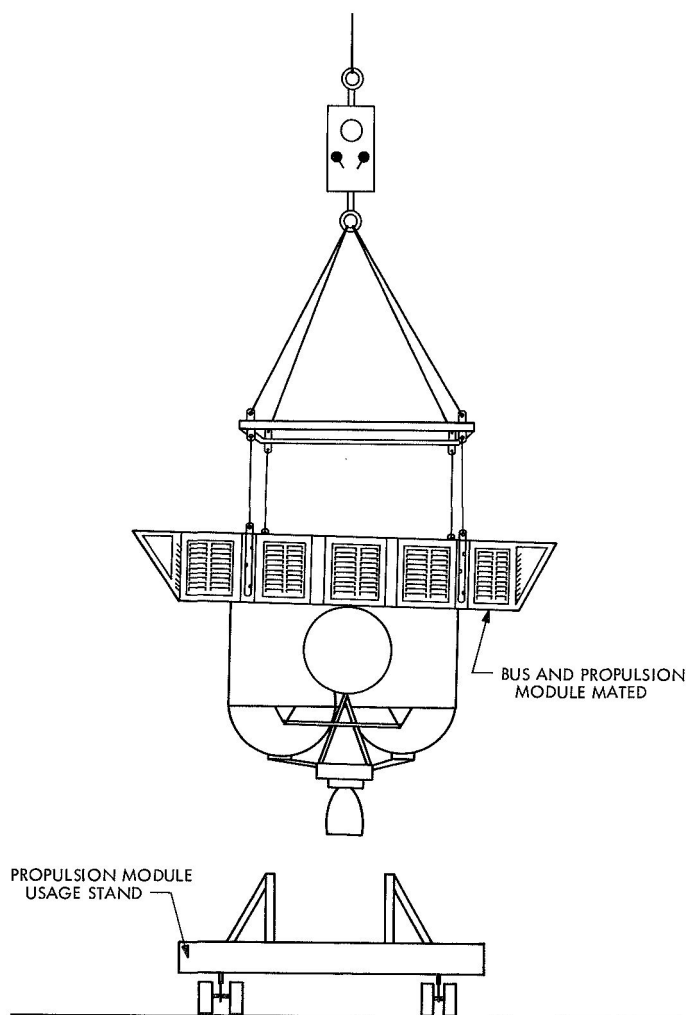


**Fig. 8. Orbiter bus to propulsion module assembly operation**



groups but for the appendage equipment, which must be attached late in the assembly sequence.

The final flight assembly sequence of the orbiter includes testing, calibration, or mechanical aligning of flight-qualified assemblies and a checkout as a system. During this period, all systems are in a most hazardous condition: propellants are loaded, pressure vessels are charged, and ordnance devices are installed.

Figure 8 illustrates the mating of the orbiter bus to the propulsion module. Figure 9 illustrates the basic structural components of the orbiter.

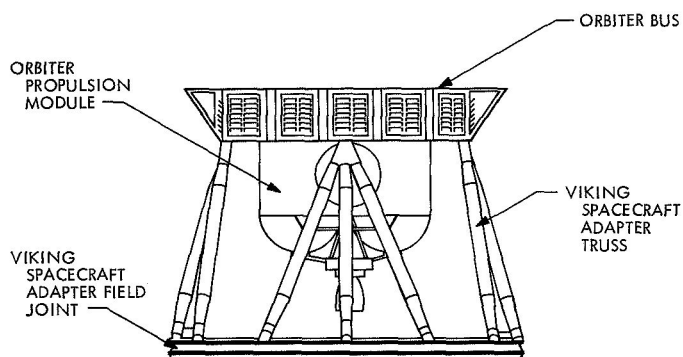


**Fig. 9. Basic orbiter structural components**

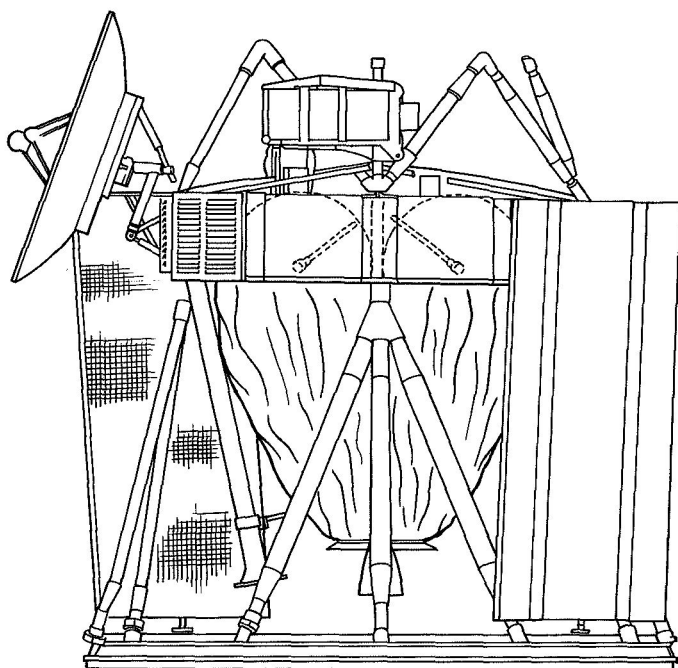
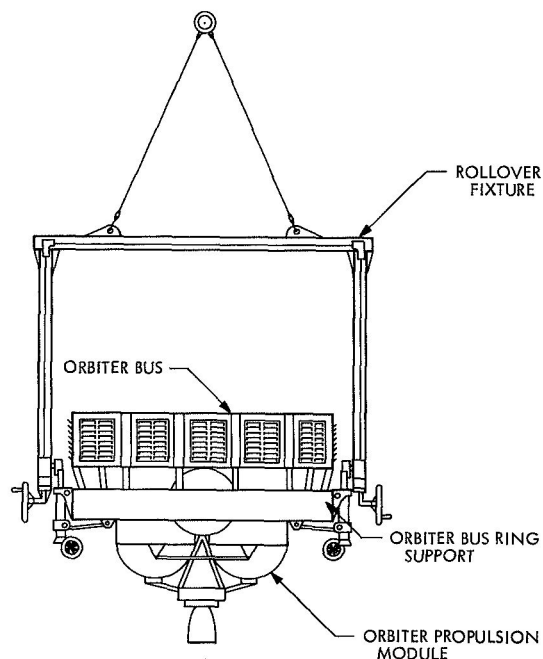


**Fig. 10. Viking orbiter launch mode configuration (solar panels removed)**

Upon completion of final assembly (Fig. 10), the orbiter is delivered to the Martin-Marietta Corp. facilities for mating with the lander/capsule. When spacecraft final assembly and testing is completed, the spacecraft is encapsulated in the nose fairing and delivered to the launch pad for mating to the launch vehicle.

*d. Major test sequences.* In the JPL space simulator test, the simulated solar source shines vertically from above. Because the cruise orientation is 180 deg from the launch orientation, this places the orbiter in an upside-

(a) STEP 1



(b) STEP 2

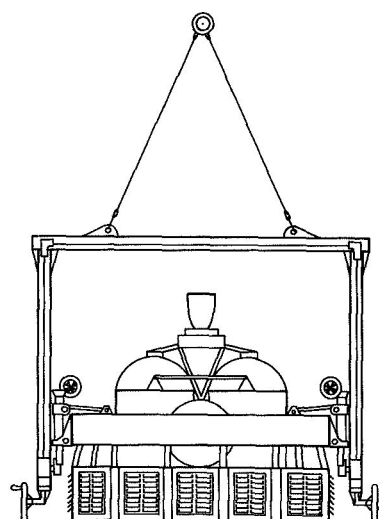


**Fig. 11. Orbiter Z-axis roll-over 180-deg operation**

down test configuration. This operation of turning the spacecraft upside down and suspending it in a vacuum chamber was previously accomplished with the *Mariner Venus 67* spacecraft; however, that spacecraft was considerably smaller than the *Viking* orbiter.

To orient the orbiter to the overhead light source, the bus (with support ring attached) is assembled to the propulsion module, which is installed in the usage stand (Fig. 8). After the roll-over fixture is attached to the bus support ring, the load is transferred to the roll-over fixture. The rotation of the assembly is accomplished by using a 50 to 1 ratio drivewheel until the 180-deg position is obtained (Fig. 11). When this operation is completed, the assembly is transferred from the roll-over fixture to a work dolly where additional assembly and testing is performed prior to installation in the simulator chamber. This sequence will first be accomplished by using the orbiter thermal control model and later the proof test model as a means of assuring a safe and well-checked technique for the flight orbiter. There is no plan to include the flight capsules in this sequence, although the option is available and will be verified during proof-test-model combined testing with the lander/capsule.

For electrical test and checkout of the orbiter in the JPL Spacecraft Assembly Facility, the system ground support equipment, sensors, stimuli, etc., are used. The systems test stand, which is used to assemble the orbiter (Fig. 12), is a portion of the systems test complex. During the testing period, the load-carrying shear plates for the electronic assemblies may be removed for troubleshooting tests. To provide support and prevent structural damage, a nonflight support is installed between the aft ring of the bus and the systems test stand. This ring makes it possible to test in a partially disassembled condition while still maintaining the structural integrity of the orbiter bus structure.

The systems test stand has a Z-axis roll and X- or Y-axis pitch capability. This is required for some of the alignment and autopilot checks. The rates of movement are compatible with the orbiter power on, power off, condition constraints.

*e. Other test sequences and equipment.* Some of the ground handling equipment required for other test sequences is listed in Table 2. Some of this equipment will

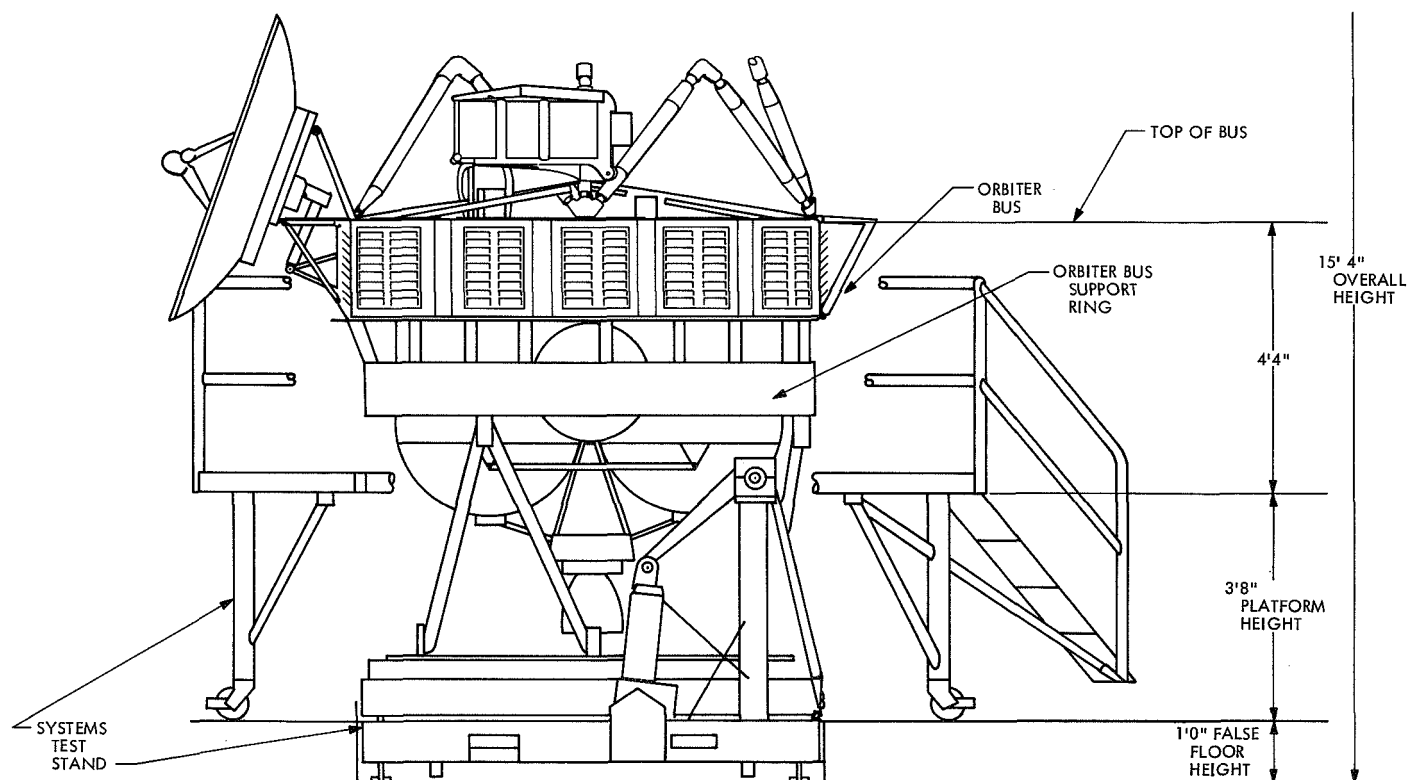


**Fig. 12. Viking orbiter installed in systems test stand**

**Table 2. Major assembly, handling, and shipping equipment**

Item	Function	Configuration	Vehicle
Orbiter Z-axis rollover assembly	To rotate Z-axis of orbiter 180 deg for proper orientation for thermal control test	Bus and propulsion module; when tested, cruise mode	Thermal control model, proof test model, flight orbiters 1 and 2
Systems test stand	For all systems testing	Bus and propulsion module plus lander	Proof test model, flight orbiters 1 and 2
Transport trailer/cover	For transport of components; always component level of assembly (never an assembled vehicle)	Bus to a given level of assembly; propulsion module in usage stand	Dynamic test model, thermal control model, proof test model, flight orbiters 1 and 2
Lifting fixture	Vertical lift operations or relocation	Bus alone to launch mode assembly	Thermal control model, dynamic test model, proof test model, flight orbiters 1 and 2
Solar panel transport trailer	Storage, transport from vendor to test site, to Air Force Eastern Test Range	Solar panel mounted in handling frame, installed in trailer (3 panels per trailer)	Dynamic test model, proof test model, flight orbiters 1 and 2
Bus, storage, and service dolly	Support bus for assembly operations	Bus and installed systems	Configuration mockup, thermal control model, dynamic test model, proof test model, flight orbiters 1 and 2
Orbiter bus ring support	Interfaces to -Z ring of bus for structural support in all modes of testing	Structure between bus and support structure (service dolly, systems test stand, transporter, etc.)	Dynamic test model, thermal control model, proof test model, flight orbiters 1 and 2
Weight and CG location fixture	To determine from the Z-axis, along the X- or Y-axis, the CG migration	Launch or cruise mode	Proof test model, flight orbiters 1 and 2
Electronic assembly installation tool	Installation of the electronic assemblies to the bus to prevent damage to components and cabling	Attaches to 14 of the 16 vertical longerons of the bus; sliding drawer concept	Proof test model, flight orbiters 1 and 2
Suspension and installation equipment for 25-ft simulator	Suspension of orbiter and lander -Z-axis vertical in 25-ft space simulator chamber	Early propulsion temperature control test configuration to Viking spacecraft test configuration	Thermal control model, proof test model, flight orbiters 1 and 2

affect flight hardware design; however, throughout developmental testing, two main constraints were required:

- (1) The ground handling equipment must not impart loads to the vehicle greater than the launch environment.
- (2) Alternate mechanical attach points must be provided for the ground handling equipment to the orbiter, thus reducing the design constraints and physical wear to the flight accessorial mounting points.

Based on the operations flow charts, it is apparent that test models experience seven or more assembly recycle operations to establish the required test configuration. The flight vehicles are subject to four recycles, with the fourth being the final flight assembly operation.

Some of the other support equipment required includes the support for the antenna test model, the support for configuration mock-up vehicles, the solar panel handling, storage and shipping trailers, and many accessorial storage and shipping containers.

## Subject Index

Subject	Pages	Subject	Pages
<b>Computer Applications and Equipment</b>		<b>Materials, Metallic</b>	
<i>Mariner</i> Mars 1971 mission-and-test		<i>Mariner</i> Mars 1971 improved television	
video system . . . . .	3-7	camera shutter materials . . . . .	22-24
<i>Mariner</i> Mars 1971 television data		<b>Mechanics</b>	
acquisition for image processing . . . . .	7-10	<i>Mariner</i> Mars 1971 flight loads analysis . . . . .	24-25
<b>Control and Guidance</b>		<b>Mechanisms</b>	
<i>Mariner</i> Mars 1971 attitude control		<i>Mariner</i> Mars 1971 improved television	
performance in commanded turn mode		camera shutter . . . . .	22-24
of operation . . . . .	10-15	<b>Photography</b>	
<i>Mariner</i> Mars 1971 Canopus tracker . . . . .	15-18	<i>Mariner</i> Mars 1971 mission-and-test	
<i>Mariner</i> Mars 1971 sun sensors . . . . .	18-21	video system . . . . .	3-7
automatic sun occultation-sun acquisition		<i>Mariner</i> Mars 1971 television data	
control for <i>Viking</i> orbiter system . . . . .	31-34	acquisition for image processing . . . . .	7-10
<b>Electronic Components and Circuits</b>		<i>Mariner</i> Mars 1971 improved television	
<i>Mariner</i> Mars 1971 Canopus tracker . . . . .	15-18	camera shutter . . . . .	22-24
<i>Mariner</i> Mars 1971 sun sensors . . . . .	18-21	<b>Propulsion, Liquid</b>	
<b>Fluid Mechanics</b>		<i>Mariner</i> Mars 1971 pressurant	
<i>Mariner</i> Mars 1971 pressurant relief plume		relief assembly . . . . .	26-29
flow field definition . . . . .	26-29	<b>Structural Engineering</b>	
<b>Launch Operations</b>		<i>Mariner</i> Mars 1971 flight loads analysis . . . . .	24-25
<i>Viking</i> orbiter system ground handling . . . . .	37-41	<b>Temperature Control</b>	
<b><i>Mariner</i> Mars 1971 Project</b>		thermal design for <i>Viking</i> orbiter system . . . . .	34-37
project description and status . . . . .	1-2	<b>Test Facilities and Equipment</b>	
mission-and-test video system . . . . .	3-7	<i>Viking</i> orbiter system test equipment . . . . .	37-41
television data acquisition for image		<b><i>Viking</i> Project</b>	
processing . . . . .	7-10	project description and status . . . . .	30-31
attitude control performance in commanded		automatic sun occultation-sun acquisition	
turn mode of operation . . . . .	10-15	control for orbiter system . . . . .	31-34
Canopus tracker . . . . .	15-18	thermal design for orbiter system . . . . .	34-37
sun sensors . . . . .	18-21	orbiter system ground handling and	
improved television camera shutter . . . . .	22-24	assembly equipment . . . . .	37-41
flight loads analysis . . . . .	24-25		
pressurant relief assembly . . . . .	26-29		